

Intra-interglacial climate variability: Model simulations of Marine Isotope Stages 1, 5, 11, 13, and 15

Rima Rachmayani¹, Matthias Prange^{1,2}, and Michael Schulz^{1,2}

¹Faculty of Geosciences, University of Bremen, Klagenfurter Strasse, D-28334 Bremen, Germany

²MARUM - Center for Marine Environmental Sciences, University of Bremen, Leobener Strasse, D-28359 Bremen, Germany

1 Using the Community Climate System Model version 3
2 (CCSM3) including a dynamic global vegetation model a set
3 of 13 time slice experiments was carried out to study global
4 climate variability between and within the Quaternary inter-
5 glacial of Marine Isotope Stages (MIS) 1, 5, 11, 13, and 15.
6 The selection of interglacial time slices was based on differ-
7 ent aspects of inter- and intra-interglacial variability and as-
8 sociated astronomical forcing. The different effects of obliquity,
9 precession and greenhouse gas (GHG) forcing on global
10 surface temperature and precipitation fields are illuminated.
11 In most regions seasonal surface temperature anomalies can
12 largely be explained by local insolation anomalies induced
13 by the astronomical forcing. Climate feedbacks, however,
14 may modify the surface temperature response in specific re-
15 gions, most pronounced in the monsoon domains and the polar
16 oceans. GHG forcing may also play an important role for
17 seasonal temperature anomalies, especially in high latitudes
18 and early Brunhes interglacials (MIS 13 and 15) when GHG
19 concentrations were much lower than during the later inter-
20 glacial. High-versus-low obliquity climates are generally
21 characterized by strong warming over the Northern Hemi-
22 sphere extratropics and slight cooling in the tropics during
23 boreal summer. During boreal winter, a moderate cooling
24 over large portions of the Northern Hemisphere continents
25 and a strong warming at high southern latitudes is found.
26 Beside the well-known role of precession, a significant role
27 of obliquity in forcing the West African monsoon is iden-
28 tified. Other regional monsoon systems are less sensitive or
29 not sensitive at all to obliquity variations during interglacials.
30 Moreover, based on two specific time slices (394 and 615 kyr
31 BP) it is explicitly shown that the West African and Indian
32 monsoon systems do not always vary in concert, challeng-
33 ing the concept of a global monsoon system at astronomical
34 timescales. High obliquity can also explain relatively warm
35 Northern Hemisphere high-latitude summer temperatures de-
36 spite maximum precession around 495 kyrBP (MIS 13). It is

37 hypothesized that this obliquity-induced high-latitude warm-
38 ing may have prevented a glacial inception at that time.

1 Introduction

The Quaternary period is characterized by the cyclic growth and decay of continental ice sheets associated with global environmental changes (e.g., Lisiecki and Raymo, 2005; Tzedakis et al., 2006; Jouzel et al., 2007; Lang and Wolff, 2011). While it is commonly accepted that the transitions between glacial and interglacial stages are ultimately triggered by varying astronomical insolation forcing (Hays et al., 1976), climate research is just beginning to understand the internal climate feedbacks that are required to shift the Earth system from one state to the other (e.g., van Nes et al., 2015). The astronomical forcing, with its characteristic periods of ca. 400 and 100 kyr (eccentricity), 41 kyr (obliquity), and ca. 19 and 23 kyr (precession) as in Berger (1978), also acts as an external driver for long-term climate change within the interglacials (i.e. the long-term intra-interglacial climate variability) and likely contributes to interglacial diversity since the evolution of astronomical parameters differs between all Quaternary interglacial stages (cf. Tzedakis et al., 2009; Yin and Berger, 2015). Understanding both interglacial climate diversity and intra-interglacial variability helps to estimate the sensitivity of the Earth system to different forcings and to assess the rate and magnitude of current climate change relative to natural variability.

Numerous interglacial climate simulations have been performed in previous studies using Earth system models of intermediate complexity (e.g., Kubatzki et al., 2000; Crucifix and Loutre, 2002; Loutre and Berger, 2003; Yin and Berger, 2012, 2015). While the present and the last interglacial have also been extensively investigated with fully coupled atmosphere-ocean general circulation models (e.g., Braconnot et al., 2007; Lunt et al., 2013), earlier interglacial periods have received much less attention by climate modellers. Coupled general circulation model (CGCM) studies of ear-

73 lier interglacial climates have recently been performed for 128
 74 Marine Isotope Stage (MIS) 11 (Milker et al., 2013; Kleinen 129
 75 et al., 2014) and MIS 13 (Muri et al., 2013). Using the 130
 76 CGCM CCSM3 (Community Climate System Model version 131
 77 3), Herold et al. (2012) presented a set of interglacial climate 132
 78 simulations comprising the interglaciations of MIS 1, 5, 9, 133
 79 11 and 19. Their study, however, focussed on peak inter- 134
 80 glacial forcing (i.e. Northern Hemisphere summer occurring 135
 81 at perihelion) and intercomparison of interglacials (i.e. inter- 136
 82 glacial diversity) only. In particular, they found that, compar- 137
 83 ed to the other interglacials, MIS 11 exhibits the closest 138
 84 resemblance to the present interglacial, especially during bo-
 85 real summer.

86 Here, we present a different and complementary CGCM 139
 87 (CCSM3) study which takes intra-interglacial climate vari- 140
 88 ability into account by simulating two or more time slices 141
 89 for each interglacial stage of MIS 1, 5, 11, 13, and 15. For 142
 90 the interglacial of MIS 5 (Last Interglacial, MIS 5e; ca. 130- 143
 91 115 kyr ago), proxy data suggest a peak global mean tem- 144
 92 perature of about 1° C higher than during the pre-industrial 145
 93 period (e.g., Otto-Bliesner et al., 2013; Dutton et al., 2015). 146
 94 The maximum global mean sea-level has been estimated to 147
 95 6-9 m above the present-day level (Kopp et al., 2009; Dutton 148
 96 and Lambeck, 2012; Dutton et al., 2015). The interglacial of 149
 97 MIS 11 was unusually long, about 30,000 years (ca. 425-395 150
 98 kyr ago). Global average temperatures of MIS 11 are highly 151
 99 uncertain, but a peak global mean temperature of up to 2° C 152
 100 relative to pre-industrial cannot be ruled out (Lang and Wolff, 153
 101 2011; Dutton et al., 2015). Maximum global mean sea-level 154
 102 may have been 6-13 m higher than today (Raymo and Mitro- 155
 103 vica, 2012; Dutton et al., 2015). Interglacials before MIS 11 156
 104 (early Brunhes interglacials), like MIS 13 and 15, are gener- 157
 105 ally characterized by lower global mean temperatures, larger 158
 106 continental ice-sheets, lower global sea level and lower atmo- 159
 107 spheric greenhouse gas (GHG) concentrations relative to the 160
 108 more recent interglacials (e.g., Yin and Berger, 2010; Lang
 109 and Wolff, 2011; Dutton et al., 2015).

110 The goal of this study is to disentangle the effects of obliq- 161
 111 uity, precession and GHG on global surface climate. Our 162
 112 selection of interglacial time slices takes into account dif- 163
 113 ferent aspects of inter- and intra-interglacial variability and 164
 114 associated astronomical forcing. As such, our approach dif- 165
 115 fers from and complements previous model studies that fo- 166
 116 cussed on peak interglacial forcing and intercomparison of
 117 interglacials (Yin and Berger, 2012; Herold et al., 2012). The 167
 118 selection of the time slices is described in detail in Section
 119 2.3. 168

120 In contrast to previously performed climate model exper- 169
 121 iments with idealized astronomical forcing, in which obliq- 170
 122 uity and precession have usually been set to extreme values 171
 123 (e.g., Tuenter et al., 2003; Mantsis et al., 2011, 2014; Erb 172
 124 et al., 2013; Bosmans et al., 2015), our analyzes are based 173
 125 on realistic astronomical configurations. We note that real- 174
 126 istic and idealized forcing experiments are equally important 175
 127 and complementary. Idealized experiments provide impor- 176

tant insight into the climate system's response to astronomi-
 cal forcing. However, since this response may be non-linear,
 using extreme values of astronomical parameters in ideal-
 ized experiments may hide important aspects of astronomi-
 cal forcing. Obviously, realistically forced experiments have
 a stronger potential for model-data comparison.

Special focus is on the sensitivity of the West African and
 Indian monsoon systems to obliquity and precession forcing.
 In particular, the applicability of the global monsoon concept
 (Trenberth et al., 2000; Wang et al., 2014) will be tested for
 astronomical timescales.

2 Experimental setup

2.1 Model description

We use the fully coupled climate model CCSM3 with the
 atmosphere, ocean, sea-ice and land-surface components in-
 teractively connected by a flux coupler (Collins et al., 2006).
 We apply the low-resolution version of the model (Yeager
 et al., 2006) which enables us to simulate a large set of time
 slices. In this version, the resolution of the atmosphere is
 given by T31 spectral truncation (3.75° transform grid) with
 26 layers, while the ocean model has a nominal horizontal
 resolution of 3° (as has the sea-ice component) with 25 lev-
 els in the vertical. The land model shares the same horizon-
 tal grid with the atmosphere and includes components for
 biogeophysics, biogeochemistry, the hydrological cycle as
 well as a Dynamic Global Vegetation Model (DGVM) based
 on the Lund-Potsdam-Jena (LPJ)-DGVM (Sitch et al., 2003;
 Levis et al., 2004; Bonan and Levis, 2006). The DGVM
 predicts the distribution of 10 plant functional types (PFT)
 which are differentiated by physiological, morphological,
 phenological, bioclimatic, and fire-response attributes (Levis
 et al., 2004). In order to improve the simulation of land-
 surface hydrology and hence the vegetation cover, new pa-
 rameterizations for canopy interception and soil evaporation
 were implemented into the land component (Oleson et al.,
 2008; Handiani et al., 2013; Rachmayani et al., 2015). PFT
 population densities are restored annually, while the land and
 atmosphere models are integrated with a 30 minutes time
 step.

2.2 Setup of experiments

To serve as a reference climatic state, a standard pre-
 industrial (PI) control simulation was carried out follow-
 ing PMIP (Paleoclimate Modelling Intercomparison Project)
 guidelines with respect to the forcing (e.g., Braconnot et al.,
 2007). The PI boundary conditions include astronomical pa-
 rameters of 1950 AD, atmospheric trace gas concentrations
 from the 18th century (Table 1) as well as pre-industrial dis-
 tributions of atmospheric ozone, sulfate aerosols, and car-
 bonaceous aerosols (Otto-Bliesner et al., 2006). The solar

constant is set to 1365 Wm^{-2} . The PI control run was inte-
grated for 1000 years starting from modern initial conditions,
except for the vegetation which starts from bare soil.

In total, 13 interglacial time slice experiments were carried
out, all branching off from year 600 of the PI spin-up run and
running for 400 years each. Note that the present study only
focusses on the surface climate, for which this spin-up time
should be sufficient, whereas the deep ocean usually needs
more time to adjust to changes in forcing (Renssen et al.,
2006).

Boundary conditions for the selected time slices which are
spanning the last 615 kyr comprise astronomical parameters
(Berger, 1978) and GHG concentrations as given in Table 1,
while other forcings (ice sheet configuration, ozone distribu-
tion, sulfate aerosols, carbonaceous aerosols, solar constant)
were kept as in the PI control run. The mean of the last 100
simulation years of each experiment was used for analysis.

We note that a fixed calendar based on a 365-day year is
used for all experiments (Joussame and Braconnot, 1997;
Chen et al., 2011). The greatest calendar-biases are known
to occur in boreal fall, whereas the effects in boreal summer
and winter (the seasons discussed in the present study) are
generally small (e.g., Timm et al., 2008).

2.3 Selection of interglacial time slices

For MIS 1, the mid-Holocene time slice of 6 kyrBP using
standard PMIP forcing (Braconnot et al., 2007) was com-
plemented by an early-Holocene 9 kyrBP simulation when
Northern Hemisphere summer insolation was close to max-
imum (Fig. 1). Two time slices, 125 and 115 kyrBP, were
also chosen for the last interglacial (MIS 5e). Similar to
9 kyrBP, the 125 kyrBP time slice is also characterized by
nearly peak interglacial forcing, although the MIS 5 insola-
tion forcing is stronger due to a greater eccentricity of the
Earth's orbit. Moreover, the global benthic $\delta^{18}\text{O}$ stack is
at minimum around 125 kyrBP (Lisiecki and Raymo, 2005).
By contrast, boreal summer insolation is close to minimum
at 115 kyrBP, which marked the end of MIS 5e (Fig. 1).
GHG concentrations for the MIS 5 time slices were taken as
specified by PMIP-3 (Lunt et al., 2013).

For the unusually long interglacial of MIS 11 (e.g., Milker
et al., 2013) three time slices were chosen, 394, 405, and
416 kyrBP. The middle time slice (405 kyrBP) coincides
with the $\delta^{18}\text{O}$ minimum of MIS 11 (Lisiecki and Raymo,
2005; Milker et al., 2013). The time slices of 394 and
416 kyrBP are characterized by almost identical precession
and similar GHG concentrations (Table 1), but opposite ex-
tremes of obliquity (maximum at 416 kyrBP, minimum at
394 kyrBP; Fig. 1). This allows to study the quasi-isolated
effect of obliquity forcing (Berger, 1978) during MIS 11 by
directly comparing the results of these two time slices. As
opposed to idealized simulations of obliquity forcing (e.g.,
Tuenter et al., 2003; Mantsis et al., 2011, 2014; Erb et al.,
2013) our approach considers quasi-realistic climate states of

the past using realistic forcings. In the same vein, time slices
for MIS 13 have been chosen. Obliquity is at maximum at
495 kyrBP and at minimum at 516 kyrBP, while precession
is almost identical. Unlike the 394 and 416 kyrBP time slices
of MIS 11 which are characterized by intermediate preces-
sion values, precession is at maximum at 495 and 516 kyrBP,
i.e. Northern Hemisphere summer occurs at aphelion caus-
ing weak insolation forcing (Yin et al., 2009). In addition,
the 504 kyrBP time slice was picked because of peak North-
ern Hemisphere summer insolation forcing, while obliquity
has an intermediate value (Fig. 1).

Finally, two time slice experiments were performed
for MIS 15 to assess the climatic response to minimum
(579 kyrBP) and maximum (609 kyrBP) precession. Ac-
cordingly, Northern Hemisphere summer insolation is near
maximum and minimum at 579 and 609 kyrBP, respec-
tively. In addition, a third MIS 15 experiment was carried out
(615 kyrBP) with insolation forcing in between the two oth-
ers (Fig. 1). Moreover, the 615 kyrBP time slice has a very
special seasonal insolation pattern as we will see in the next
section. All three MIS 15 time slices coincide with minimum
 $\delta^{18}\text{O}$ values (Lisiecki and Raymo, 2005).

Table 1 summarizes the GHG forcing of all experiments
with values based on Lüthi et al. (2008), Louergue et al.
(2008), and Schilt et al. (2010) using the EPICA Dome C
timescale EDC3, except for the MIS 1 and MIS 5 experi-
ments, where GHG values were chosen following the PMIP
guidelines (see above). We note that due to the uneven distri-
bution of methane sources and sinks over the latitudes, val-
ues of atmospheric CH_4 concentration derived from Antarc-
tic ice cores present a lower estimate of global CH_4 con-
centration. We further note that some results from the MIS
1 (6 and 9 kyrBP), MIS 5 (125 kyrBP), and MIS 11 (394,
405, and 416 kyrBP) experiments were previously published
(Lunt et al., 2013; Milker et al., 2013; Kleinen et al., 2014;
Rachmayani et al., 2015).

2.4 Insolation anomalies

Annual cycles of the latitudinal distribution of insolation at
the top of the atmosphere (as anomalies relative to PI) are
shown in Fig. 2 for each experiment. The insolation pat-
terns can be divided into three groups which differ in their
seasonal distribution of incoming energy. Group I is charac-
terized by high Northern Hemisphere summer insolation as
exhibited for the 6 and 9 kyrBP (MIS 1), 125 kyrBP (MIS
5), 405 and 416 kyrBP (MIS 11), 504 kyrBP (MIS 13), and
579 kyrBP (MIS 15) time slices. In most (but not all, see be-
low) cases this is due to an astronomical configuration with
northern summer solstice at or close to perihelion. Group II
comprises anomalies with low boreal summer insolation as
shown for 115 kyrBP (MIS 5), 495 and 516 kyrBP (MIS 13),
and 609 kyrBP (MIS 15). In these cases, northern winter sol-
stice is near perihelion. Group III is characterized by changes
in the sign of the Northern Hemisphere insolation anoma-

Stage	Time slice (ka BP)	CO ₂ (ppmv)	CH ₄ (ppbv)	N ₂ O (ppbv)
MIS 1	0	280	760	270
	6	280	650	270
	9	265	680	260
MIS 5	115	273	472	251
	125	276	640	263
MIS 11	394	275	550	275
	405	280	660	285
	416	275	620	270
MIS 13	495	240	487	249
	504	240	525	278
	516	250	500	285
MIS 15	579	252	618	266
	609	259	583	274
	615	253	617	274

Table 1. Atmospheric GHG concentrations used in the interglacial experiments.

lies from spring to summer and consists of two dates (394 and 615 kyrBP). At 394 (615 kyrBP) the insolation anomaly spring-to-summer change is from positive (negative) to negative (positive). In these cases, spring equinox (394 kyrBP) or fall equinox (615 kyrBP) are close to perihelion.

3 Results

3.1 JJAS surface temperature anomalies

The response of boreal summer (June–July–August–September, JJAS) surface temperature to the combined effect of insolation and GHG in all individual climates (Fig. 3) shows warm conditions (relative to PI) over most parts of the continents in Group I (6, 9, 125, 405, 416, 504, and 579 kyrBP) with the three warmest anomalies at 9, 125, and 579 kyrBP. The warm surface conditions can largely be explained by the immediate effect of high summer insolation and a reduction of the Northern Hemisphere sea-ice area by about 15–20% (not shown) relative to PI. The large thermal capacity of the ocean explains a larger temperature response over land than over the ocean (Herold et al., 2012; Nikolova et al., 2013). Simulated cooling over North Africa (10–25° N) and India in the Group I experiments is caused by enhanced monsoonal rainfall in these regions, which is associated with increased cloud cover, i.e. reduced short-wave fluxes, and enhanced land surface evapotranspiration, i.e. greater latent cooling (e.g., Braconnot et al., 2002, 2004; Zheng and Braconnot, 2013). Cooling in some parts of the Southern Ocean in most Group I experiments is likely attributable to an austral summer remnant effect of local insolation (see below) as in Yin and Berger (2012). The 416 kyrBP time slice, however, differs from the other Group I members by anomalously cold conditions over the Southern Hemisphere continents. Again, this behaviour can be explained by the immediate effect of the insolation, which shows negative anomalies in the Southern Hemisphere during the JJAS

season (Fig. 2). As such, the 416 kyrBP time slice must be considered a special case in Group I. While high Northern Hemisphere summer insolation is related to low precession in most Group I members, positive anomalies of Northern Hemisphere summer insolation at 416 kyrBP are attributable to a maximum in obliquity (Fig. 1), yielding the Northern-versus-Southern Hemisphere insolation contrast.

In contrast to Group I, Group II climates exhibit anomalously cold JJAS surface temperatures globally with the three coldest anomalies at 115, 516, and 609 kyrBP. Again, the temperature response can largely be explained by the direct response to insolation forcing, amplified in high latitudes by an increase of the sea-ice cover (about 5% in the Arctic compared to PI). Due to a particular combination of high precession and eccentricity with low obliquity the insolation forcing and surface temperature response is strongest for the 115 kyrBP time slice. Group II warming in the North African and Indian monsoon regions is associated with increased aridity and reduced cloudiness.

Group III climates (394 and 615 kyrBP) show rather complex temperature anomaly patterns, especially in the tropics. In the 394 kyrBP time slice, however, northern continental regions show a distinct cooling, whereas continental regions exhibit an overall warming in the Southern Hemisphere (except for Antarctica). To a large extent, the 394 kyrBP time slice shows a reversed JJAS temperature anomaly pattern compared to the 416 kyrBP simulation over the continental regions, except for Antarctica.

3.2 DJF surface temperature anomalies

Boreal winter (December–January–February, DJF) surface temperature anomalies are presented in Fig. 4. Generally low DJF insolation in Group I time slices (Fig. 2) results in anomalously cold surface conditions over most of the globe, particularly strong in the 579 kyrBP (MIS 15) time slice. However, anomalously warm conditions in the Arctic stand

in contrast to the global DJF cooling at 6, 9, 125, 405, and 416 kyrBP. The Arctic warming is due to the remnant effect of the polar summer insolation through ocean–sea ice feedbacks (Fischer and Jungclaus, 2010; Herold et al., 2012; Yin and Berger, 2012; Kleinen et al., 2014). Anomalous short-wave radiation during the Arctic summer leads to enhanced melting of sea ice and warming of the upper polar ocean. The additional heat received by the upper ocean delays the formation of winter sea ice, reduces its thickness and finally leads to a warming of the winter surface atmospheric layer by enhanced ocean heat release (Yin and Berger, 2012). Arctic winter warming is not present in the 504 kyrBP (MIS 13) and 579 kyrBP (MIS 15) time slices in Group I, where the summer remnant effect in the Arctic is probably masked by a global cooling that is induced by low GHG concentrations typical for early Brunhes (MIS 13 and before) interglacials.

To a large extent, DJF surface temperature anomaly patterns are reversed in Group II with warming over most continental regions. Moreover, the summer remnant effect reverses to a substantial cooling in the Arctic region. Temperature anomaly patterns in Group III are, again, rather complex. Interestingly, most Northern Hemisphere continental regions remain relatively cold during boreal winter (as in summer) in the 394 kyrBP simulation. Relatively low GHG concentrations, especially CH₄, contribute to the year-round extratropical cooling in this time slice.

3.3 JJAS precipitation anomalies

Boreal summer precipitation shown in Fig. 5 exhibits intensified rainfall in the monsoon belt from North Africa to India, via the Arabian Peninsula, in all Group I simulations in response to high summer insolation (Prell and Kutzbach, 1987; de Noblet et al., 1996; Tuenter et al., 2003; Braconnot et al., 2007). By contrast, the same monsoon regions experience anomalously dry conditions in the Group II (low boreal summer insolation) experiments. The most interesting results regarding the tropical rainfall response to astronomical forcing appear in Group III, where the monsoonal precipitation anomalies show opposite signs in North Africa (Sahel region) and India.

Table 2 summarizes the summer monsoonal rainfall amounts for the North African (20° W–30° E; 10–25° N) and Indian (70–100° E; 10–30° N) regions. Highest rainfall in the North African monsoon region occurs in the 9, 125, 504, and 579 kyrBP time slice runs (all Group I) associated with low precession values (Fig. 1). Driest conditions occur at 115, 495, 516, and 609 kyrBP (all Group II) associated with precession maxima (Fig. 1). As in North Africa, Group I (Group II) experiments exhibit anomalously wet (dry) monsoon conditions in India.

3.4 Net Primary Production (NPP) anomalies

Vegetation responds to changes in surface temperature and precipitation and, in certain regions, may feedback to the climate (cf. Rachmayani et al., 2015). Figure 6 shows the simulated changes in NPP, reflecting increase/decrease and expansion/retreat of vegetation covers, relative to PI. In high Arctic latitudes, NPP increases in the Group I simulations, except for 405 kyrBP where temperature changes are probably too small to substantially affect the vegetation. By contrast, Arctic NPP declines in the Group II experiments, albeit only in the easternmost part of Siberia in the 495 kyrBP experiment. A substantial decline of Arctic NPP is also simulated for 394 kyrBP (Group III). In the tropical regions, vegetation changes are mostly governed by precipitation. Consequently, enhanced rainfall results in increased NPP over North Africa, the Arabian Peninsula and India in all Group I experiments. In North Africa increased NPP is associated with a northward shift of the Sahel–Sahara boundary. The largest shifts are simulated for 125 and 579 kyrBP in accordance with maximum North African rainfall anomalies. In these experiments, a complete greening of the Arabian Desert is simulated. Opposite NPP anomalies in the tropical monsoon regions are simulated in the Group II experiments. In Group III, NPP increases result from anomalously high rainfall in North Africa (615 kyrBP) or India (394 kyrBP).

3.5 Climatic effects of obliquity variations during MIS 11 and MIS 13

The MIS 11 time slices 394 and 416 kyrBP show opposite obliquity extremes (at similar precession), as do the MIS 13 time slices 495 and 516 kyrBP (Fig. 1). Insolation differences between the high obliquity (416, 495 kyrBP) and low obliquity (394, 516 kyrBP) cases (i.e. 416 minus 394 and 495 minus 516 kyrBP) are displayed in Fig. 7. The effect of high obliquity is to strengthen the seasonal insolation cycle. At low latitudes, the effect of obliquity on insolation is small.

For the maximum obliquity time slices (416 and 495 kyrBP) relatively high boreal summer insolation directly translates into positive surface temperature anomalies over Northern Hemisphere continents, except for the low latitudes where reduced local insolation (especially in the MIS 13 case) and higher monsoon rainfall (especially in the MIS 11 case, see below) lead to surface cooling (Fig. 8a,b). By contrast, receiving anomalously low insolation during austral winter, Southern Hemisphere continents exhibit anomalously cold surface temperatures. For the 416–394 kyrBP case, however, the Antarctic continent and the Southern Ocean show large-scale warming during the JJAS season, which can be attributed to a south polar summer remnant effect as the austral summer insolation anomaly is extremely high in this experiment (Fig. 7a). Higher GHG concentrations at 416 compared to 394 kyrBP may add to this warming. Owing to a smaller south polar summer insolation anomaly (Fig. 7)

Stage	Time slice	North Africa (mm day ⁻¹)	North Africa Anomaly (mm day ⁻¹)	India (mm day ⁻¹)	India Anomaly (mm day ⁻¹)
MIS 1	0 ka	2.44±0.04		6.59±0.12	
	6 ka	3.41±0.04	0.97	6.91±0.10	0.32
	9 ka	3.71±0.04	1.27	7.36±0.08	0.77
MIS 5	115 ka	1.59±0.02	-0.85	5.90±0.15	-0.69
	125 ka	3.79±0.04	1.35	7.26±0.07	0.67
MIS 11	394 ka	2.37±0.04	-0.07	6.92±0.12	0.33
	405 ka	3.20±0.04	0.76	6.95±0.11	0.36
	416 ka	3.06±0.04	0.62	7.13±0.12	0.54
MIS 13	495 ka	1.91±0.04	-0.53	6.11±0.13	-0.48
	504 ka	3.72±0.04	1.28	7.11±0.08	0.52
	516 ka	1.88±0.04	-0.56	6.22±0.13	-0.37
MIS 15	579 ka	3.77±0.04	1.33	7.72±0.07	1.13
	609 ka	1.49±0.02	-0.95	6.10±0.13	-0.49
	615 ka	3.21±0.04	0.77	6.27±0.13	-0.32

Table 2. Summer (JJAS) precipitation over North Africa (20° W–30° E and 10–25° N) and over India (70° E–100° E and 10–30° N) along with anomalies relative to PI. Absolute precipitation values are given with standard error (2 σ) based on 100 simulation years of each experiment.

the summer remnant effect is smaller in the 495–516 kyrBP case and even surpassed by anomalously low GHG forcing in the 495 kyrBP time slice, leading to negative austral winter temperature anomalies in the Southern Ocean and Antarctica (Fig. 7b).

During boreal winter, Northern Hemisphere continents show large-scale cooling in response to high obliquity (and hence relatively low insolation), except for the Arctic realm where the summer remnant effect results in substantial positive surface temperature anomalies (Fig. 8c and d). During the same season (DJF) anomalously high insolation causes surface warming in the Southern Hemisphere in response to high obliquity. As a general pattern in the annual mean, maximum-minus-minimum obliquity forcing causes anomalous surface warming at high latitudes and surface cooling at low latitudes caused by seasonal and annual insolation anomalies in combination with climate feedbacks like the polar summer remnant effect and monsoon rainfall.

Despite the weak insolation signal at low latitudes, substantial obliquity-induced changes in tropical precipitation are simulated (Fig. 8e and f). The strongest signal is found in the North African monsoon region in the MIS 11 experiments, where greater JJAS precipitation occurs during maximum obliquity at 416 kyrBP than during the obliquity minimum at 394 kyrBP. A positive Sahel rainfall anomaly is also found in the MIS 13 experiments (495–516 kyrBP), but much weaker than in the MIS 11 case (416–394 kyrBP). We suppose that the obliquity-induced increase in North African monsoonal rainfall is counteracted by the high precession at 495 kyrBP that tends to weaken the monsoon. Considering the spatiotemporal insolation patterns (Fig. 7) the Northern Hemisphere tropical summer insolation anomaly is less negative and the meridional summer insolation gradient anomalies are generally greater in the 416–394 kyrBP case compared to the 495–516 kyrBP case. Both features of the insolation

anomaly favor a strong North African monsoon (see Discussion).

3.6 Evaluating the climatic effects of astronomical and GHG forcings through correlation maps

In order to evaluate the climatic effects of obliquity, precession and GHG concentrations, linear correlations between the individual forcing parameters and climatic fields (surface temperature, precipitation) were calculated from the 14 time slice experiments (13 interglacial time slices plus PI). To this end, each climate variable (temperature, precipitation) was averaged over the last 100 years of each experiment. Linear correlation coefficients between a climatological variable and a forcing parameter (obliquity, precession, GHG radiative forcing) were calculated at each grid point. Significance of correlations was tested by a two-sided Student's *t* test with 95% confidence level. Total radiative forcing from CO₂, CH₄, and N₂O in each experiment was calculated based on a simplified expression given in Table 3 (IPCC, 2001).

Figure 9 shows the corresponding correlation maps for annual mean, boreal summer, and boreal winter surface temperature. As expected, GHG forcing is positively correlated with surface temperature over most regions of the globe (Fig. 9a), which is particularly pronounced in the annual mean. For the seasonal correlation maps (boreal summer and winter) the correlation coefficients are smaller because of the dominant impact of obliquity and precession forcing.

As already described in the previous subsection, the general surface temperature pattern of high obliquity forcing is warming at high latitudes and cooling at low latitudes (Fig. 9b). High precession (northern solstice near aphelion) leads to boreal summer surface cooling over most extratropical regions (Fig. 9c). However, surface warming occurs in some tropical regions as a response to weaker monsoons. During boreal winter, anomalously high insolation causes anoma-

Trace gas	Simplified expression Radiative forcing, ΔF (Wm^{-2})	Constants
CO ₂	$\Delta F = \alpha(g(C) - g(C_0))$ where $g(C) = \ln(1 + 1.2C + 0.005C^2 + 1.4 \times 10^{-6}C^3)$	$\alpha = 3.35$
CH ₄	$\Delta F = \alpha(\sqrt{M} - \sqrt{M_0}) - (f(M, N) - f(M_0, N_0))$	$\alpha = 0.036$
N ₂ O	$\Delta F = \alpha(\sqrt{N} - \sqrt{N_0}) - (f(M, N) - f(M_0, N_0))$ where $f(M, N) = 0.47 \ln[1 + 2.01 \times 10^{-5}(MN)^{0.75} + 5.31 \times 10^{-15}M(MN)^{1.52}]$	$\alpha = 0.12$

Table 3. Simplified expressions for calculation of radiative forcing due to CO₂, CH₄, N₂O. C is CO₂ in ppmv, M is CH₄ in ppbv, N is N₂O in ppbv. The subscript 0 denotes the unperturbed GHG concentration of PI.

lous surface warming except in the Arctic (due to the summer remnant effect) and northern Australia (due to a stronger regional monsoon).

Correlation maps for annual mean, boreal summer, and boreal winter precipitation are shown in Fig. 10. GHG radiative forcing exhibits no clear response in precipitation except for the high latitudes where the hydrologic cycle accelerates with higher GHG concentrations (Fig. 10a). Since the GHG variations are relatively small, the effects of astronomical forcing on the monsoons are way larger than the effects of GHG variations during the interglacials. Arctic precipitation is also amplified by high obliquity during summer (Fig. 10b). Obliquity also strengthens the monsoonal rainfall in North Africa (Sahel region), whereas no effect of obliquity can be detected for the Australian monsoon. The sensitivity of other monsoon systems to obliquity changes is also weak or even absent in our experiments. The most robust response of the hydrologic cycle is found for precession (Fig. 10c). In particular, high precession reduces summer rainfall in the monsoon belt from North Africa to India as well as in the Arctic realm. East Asian rainfall shows a somewhat heterogeneous pattern and is, in general, only weakly coupled with the Indian and African monsoons. This finding is consistent with a recent model intercomparison study by Dallmeyer et al. (2015). During boreal winter, the hydrologic cycle strengthens in the Arctic and Antarctic regions, while Southern Hemisphere monsoon systems amplify resulting in enhanced rainfall over South America, southern Africa, and northern Australia in response to high precession. We note that these monsoonal rainfall changes go along with distinct surface temperature signals in the annual mean (Fig. 9c).

4 Discussion

While most time slices presented in this study were simulated for the first time using a comprehensive CGCM, the 6, 115 and 125 kyrBP time slices have been extensively studied in previous model studies. In general, the CCSM3 results are in line with these previous studies in terms of large-scale temperature and precipitation patterns. Warm boreal summer conditions (relative to PI) over most parts of the continents and the Arctic are a general feature in paleoclimatic simulations of the mid-Holocene (6 kyrBP), while the North African and South Asian monsoon regions

are anomalously cold due to enhanced rainfall (Braconnot et al., 2007). Though evidenced by proxy records (e.g., McClure, 1976; Hoelzmann et al., 1998; Fleitmann et al., 2003), several models fail to simulate wetter mid-Holocene conditions over the Arabian Peninsula (cf. <https://pmip3.lscce.fr/database/maps/>), while CCSM3 simulates not only enhanced rainfall but also greening of the Arabian Desert. The 125 kyrBP surface temperature pattern shows similar features than the 6 kyrBP pattern, but much more pronounced due to the larger eccentricity and hence stronger precessional forcing. However, compared to other simulations of the last interglaciation, our CCSM3 simulation produces a relatively cold MIS 5e surface climate as shown by Lunt et al. (2013). At 115 kyrBP, surface temperature anomalies show the opposite sign with dramatic cooling over the Arctic and the northern continental regions providing ideal conditions for glacial inception (e.g., Khodri et al., 2005; Kaspar and Cubasch, 2007; Jochum et al., 2012). A retreat of the vegetation at high northern latitudes tends to amplify the insolation-induced cooling (cf. Gallimore and Kutzbach, 1996; Meissner et al., 2003).

A recent simulation of the MIS 13 time slice at 506 kyrBP using the CGCM HadCM3 (Muri et al., 2013) can be compared to our 504 kyrBP time slice using CCSM3. Global patterns of surface temperature anomalies (relative to PI) are remarkably similar in the two different simulations with warm anomalies over all continents (except for the North African and South Asian monsoon regions) in boreal summer and worldwide cold anomalies during boreal winter. Moreover, both simulations show anomalously high boreal summer precipitation over northern South America, North and central Africa as well as the South Asian monsoon region.

Although our CCSM3 results show general agreement with other model studies, the validation of model results with data is usually not straightforward. The reader is referred to previous work where our CCSM3 simulation of 125 kyrBP (Lunt et al., 2013) as well as the MIS 11 simulations have been extensively compared to proxy data (Milker et al., 2013; Kleinen et al., 2014). Taken together, these and other studies (e.g., Lohmann et al., 2013) indicate that CGCMs tend to produce generally smaller interglacial temperature anomalies than suggested by the proxy records. So far, the reason for these discrepancies is unsolved (cf. Liu et al., 2014), but Hessler et al. (2014) pointed out that uncertainties associated with sea surface temperature reconstructions are generally

larger than interglacial temperature anomalies. Thus, currently available surface temperature proxy data cannot serve as a target for benchmarking interglacial model simulations.

Two time slices of MIS 11 (394 vs. 416 kyrBP) and two time slices of MIS 13 (495 vs. 516 kyrBP) allow the investigation of (almost pure) obliquity effects on global climate, although the GHG and precession are not exactly the same between the time slices. As such, the results from these simulations can be compared to previously performed idealized model experiments in which obliquity has been changed from maximum to minimum values (Tuenter et al., 2003; Mantsis et al., 2011; Erb et al., 2013; Bosmans et al., 2015). The common results of those idealized and our experiments can be summarized as follows. High-versus-low obliquity climates are characterized by strong warming over the Northern Hemisphere extratropics and slight cooling in the tropics during boreal summer. During boreal winter, a moderate cooling over large portions of the Northern Hemisphere continents and a strong warming at high southern latitudes is found. The obliquity-induced Northern Hemisphere summer warming appears to be of particular interest for the MIS 13 climate evolution. At 495 kyrBP, precession is at maximum, but the global benthic $\delta^{18}\text{O}$ stack by Lisiecki and Raymo (2005) does not show the expected increase towards heavier values which would indicate colder conditions and Northern Hemisphere cryosphere expansion (Fig. 1). In fact, despite high precession, the 495 kyrBP simulation exhibits the warmest Northern Hemisphere summer temperatures from all Group II experiments (Fig. 3), which can be attributed to concomitant high obliquity. We therefore hypothesize that the Northern Hemisphere summer climate at 495 kyrBP was not cold enough for ice sheets to grow and global ocean $\delta^{18}\text{O}$ to increase. We note, however, that the benthic $\delta^{18}\text{O}$ stack is subject to age model uncertainties of a few thousand years.

Moreover, our CCSM3 results as well as the studies by Tuenter et al. (2003) and Bosmans et al. (2015) suggest a significant effect of obliquity on West African monsoon rainfall despite the weak insolation signal at low latitudes. Bosmans et al. (2015) have shown that obliquity-induced changes in moisture transport towards North Africa result from changes in the meridional insolation gradient (Davis and Brewer, 2009). However, the impact of obliquity on the monsoon also depends on precession. In the 495–516 kyrBP experiment the obliquity-effect on the West African monsoon is minor, as both time slices (495 and 516 kyrBP) are characterized by precession maxima leading to extremely weak monsoonal circulation and rainfall in both cases. The existence of a ~ 41 kyr cyclicity (in addition to astronomical-related ~ 100 and 19–23 kyr cycles) in reconstructions of North African aridity during the Quaternary has usually been attributed to obliquity-forced Northern Hemisphere cryosphere effects on the monsoon climate (e.g., Bloemendal and deMenocal, 1989; deMenocal et al., 1993; Tiedemann et al., 1994; deMenocal, 1995; Kroon et al., 1998). Our model results along with the studies by Tuenter et al. (2003) and

Bosmans et al. (2015) complement this picture, showing that the direct insolation-gradient forcing associated with obliquity can contribute to West African monsoon changes without involving high-latitude remote climate forcing associated with Northern Hemisphere ice sheets.

According to the CCSM3 results, the Indian monsoon is less sensitive to direct obliquity (insolation gradient) forcing than the West African monsoon. This finding is consistent with proxy records from the Arabian Sea that show substantial 41 kyr (obliquity) periodicity only after the onset of Quaternary glacial cycles when waxing and waning of northern ice sheets could have worked as an agent for the transfer of obliquity forcing to the Indian monsoon region (Bloemendal and deMenocal, 1989). In general, it is found that the two monsoon systems do not always vary in concert. This is particularly evident in the Group III experiments (394 and 615 kyrBP) where the precipitation anomalies over North Africa and India have opposite signs (Table 2). Considering the annual insolation maps of the 394 and 615 kyr experiments (Fig. 2), West African monsoon rainfall turns out to be most sensitive to changes in summer insolation, whereas spring/early summer insolation is more important for monsoon rainfall over India. Similar results have been found by Braconnot et al. (2008). It has been argued that the reason is a resonant response of the Indian monsoon to the insolation forcing when maximum insolation anomalies occur near the summer solstice and a resonant response of the African monsoon – which has its rainfall maximum one month later in the annual cycle than the Indian monsoon – when the maximum insolation change is delayed after the summer solstice. The different responses to specific forcings and the sometimes out-of-phase behaviour of the African and Indian monsoon systems challenge the global monsoon concept – according to which all regional monsoon systems are part of one seasonally varying global-scale atmospheric overturning circulation in the tropics (Trenberth et al., 2000; Wang et al., 2014) – at astronomical timescales.

Another important result of our study is associated with obliquity forcing of high-latitude precipitation anomalies. As obliquity increases, high latitudes become warmer and the gradient in solar heating between high and low latitudes decreases, while precipitation over high-latitude continental regions increases (Fig. 10b). This result clearly contradicts the “gradient hypothesis” by Raymo and Nisancioglu (2003) according to which low obliquity would favour polar ice-sheet growth through enhanced delivery of moisture owing to an increased meridional solar heating gradient.

Since CO_2 and other GHG variations are relatively small during the interglacials, the effects of astronomical forcing on the monsoons are substantially larger. Hence, GHG forcing shows a clear response in precipitation only for the high latitudes where the hydrologic cycle accelerates with higher GHG concentrations. In the monsoon regions, interglacial rainfall variations are almost entirely controlled by astronomical forcing.

The use of a modern ice-sheet configuration for all interglacial time slice experiments, however, must be considered a limitation of the present study. Future studies should include the effects of changing ice sheets and associated meltwater fluxes in shaping interglacial climates. Large Northern Hemisphere ice sheets might have played an important role for regional and global climates especially during early Brunhes interglacials (MIS 13 and before) as suggested by, e.g., Yin et al. (2008) and Muri et al. (2013). But also during late Brunhes interglacial stages, like the Holocene, model studies suggest an influence of changing land ice on the interglacial climate evolution (Renssen et al., 2009; Marzin et al., 2013). The tremendous uncertainties regarding ice-sheet reconstructions beyond the present interglacial could be taken into account by performing sensitivity experiments.

5 Conclusions

Using CCSM3-DGVM, 13 interglacial time slice experiments were carried out to study global climate variability between and within Quaternary interglacials. The selection of interglacial time slices was based on different aspects of inter- and intra-interglacial variability and associated astronomical forcing. As such, our approach is complementary to both idealized astronomical forcing experiments (e.g., Tuenter et al., 2003; Mantsis et al., 2011, 2014; Erb et al., 2013; Bosmans et al., 2015) and climate simulations that focussed on peak interglacial forcing (Herold et al., 2012; Yin and Berger, 2012).

In this study, the different roles of obliquity, precession and GHG forcing on surface temperature and precipitation patterns have been disentangled. In most regions seasonal surface temperature anomalies could largely be explained by local insolation anomalies induced by the astronomical forcing. Climate feedbacks modify the surface temperature response in specific regions, particularly in the monsoon domains and the polar oceans. GHG forcing may also play a role for seasonal temperature anomalies, especially in high latitudes and the early Brunhes interglacials MIS 13 and 15 when GHG concentrations were much lower than during the later interglacials.

A significant role of obliquity in forcing the West African monsoon was found, whereas the Indian monsoon – as well as the other regional monsoon systems – appear to be less sensitive (or not sensitive at all) to obliquity changes during interglacials. Despite this important role of obliquity in West African monsoon variability, the response to precession is still stronger. Different responses to specific forcings and the obvious anti-phase behaviour of the African and Indian monsoon systems in the 394 and 615 kyrBP experiments, where the North African rainfall anomaly has opposite sign compared to the Indian anomaly, clearly point to the fact that the two regional monsoon systems do not always vary in concert

and challenge the global monsoon concept at the astronomical timescale.

As a general pattern in the annual mean, maximum-minus-minimum obliquity forcing causes anomalous surface warming at high latitudes and surface cooling at low latitudes caused by seasonal and annual insolation anomalies in combination with climate feedbacks like the polar summer remnant effect and monsoon rainfall. High obliquity may also explain relatively warm Northern Hemisphere high-latitude summer temperatures despite maximum precession around 495 kyrBP (MIS 13). We hypothesize that this obliquity-induced high-latitude warming may have prevented a glacial inception at that time. Moreover, our results suggest high-latitude precipitation increase with increasing obliquity, contradicting the “gradient hypothesis” by (Raymo and Nisançioğlu, 2003) according to which low obliquity would favour polar ice-sheet growth through enhanced delivery of moisture owing to an increased meridional solar heating gradient.

Future studies should include the effects of changing ice sheets and associated meltwater fluxes in shaping interglacial climates. With increasing computer power long-term transient simulations of interglacial climates will become more common. So far, transient CGCM simulations have been performed for the present (e.g., Lorenz and Lohmann, 2004; Varma et al., 2012; Liu et al., 2014) and the last interglacial (e.g., Bakker et al., 2013; Govin et al., 2014). More transient simulations of earlier interglacials, ideally with coupled interactive ice-sheet models, will help to develop a significantly deeper understanding of interglacial climate dynamics.

Acknowledgements. The study was funded by the Deutsche Forschungsgemeinschaft (DFG) through the Priority Programme INTERDYNAMIC. CCSM3 simulations were performed on the SGI Altix supercomputer of the Norddeutscher Verbund für Hoch- und Höchstleistungsrechnen (HLRN). The article processing charges for this open-access publication were covered by the University of Bremen. We would like to thank the two anonymous reviewers for their constructive suggestions and helpful comments.

References

- Bakker, P., Stone, E. J., Charbit, S., Gröger, M., Krebs-Kanzow, U., Ritz, S. P., Varma, V., Khon, V., Lunt, D. J., Mikolajewicz, U., Prange, M., Renssen, H., Schneider, B., and Schulz, M.: Last interglacial temperature evolution – a model inter-comparison, *Clim. Past*, 9, 605–619, doi:10.5194/cp-9-605-2013, 2013.
- Berger, A.: Long-term variations of daily insolation and Quaternary Climatic Changes, *J. Atmos. Sci.*, 35, 2362–2367, 1978.
- Bloemendal, J. and deMenocal, P.: Evidence for a change in the periodicity of tropical climate cycles at 2.4 Myr from whole-core magnetic susceptibility measurements, *Nature*, 342, 897–900, 1989.
- Bonan, G. B. and Levis, S.: Evaluating aspects of the Community Land and Atmosphere Models (CLM3 and CAM) using a dynamic global vegetation model, *J. Climate*, 19, 2290–2301, 2006.

- 823 Bosmans, J. H. C., Drijfhout, S. S., Tuenter, E., Hilgen, F. J., and 882
 824 Lourens, L. J.: Response of the North African summer monsoon 883
 825 to precession and obliquity forcings in the EC-Earth GCM, *Clim. 884*
 826 *Dyn.*, 44, 279–297, doi:s00382-014-2260-z, 2015. 885
- 827 Braconnot, P., Loutre, M. F., Dong, B., Joussaume, S., and 886
 828 Valdes, P.: How the simulated change in monsoon at 6kaBP is 887
 829 related to the simulation of the modern climate: results from the 888
 830 Paleoclimate Modeling Intercomparison Project, *Clim. Dyn.*, 19, 889
 831 107–121, 2002. 890
- 832 Braconnot, P., Harrison, S., Joussaume, J., Hewitt, C., Kitoh, A., 891
 833 Kutzbach, J., Liu, Z., Otto-Bleisner, B. L., Syktus, J., and We- 892
 834 ber, S. L.: Evaluation of coupled ocean-atmosphere simulations 893
 835 of the mid-Holocene, in: *Past Climate Variability Through Eu- 894*
 836 rope and Africa, edited by: Battarbee, R. W., Gasse, F., and 895
 837 Stickley, C. E., Kluwer Academic Publisher, 515–533, Dor- 896
 838 drecht, 2004. 897
- 839 Braconnot, P., Otto-Bliesner, B., Harrison, S., Joussaume, S., Pe- 898
 840 terchmitt, J.-Y., Abe-Ouchi, A., Crucifix, M., Driesschaert, E., 899
 841 Fichetef, Th., Hewitt, C. D., Kageyama, M., Kitoh, A., Laîné, A., 900
 842 Loutre, M.-F., Marti, O., Merkel, U., Ramstein, G., Valdes, P., 901
 843 Weber, S. L., Yu, Y., and Zhao, Y.: Results of PMIP2 coupled 902
 844 simulations of the Mid-Holocene and Last Glacial Maximum – 903
 845 Part I: experiments and large-scale features, *Clim. Past*, 3, 261– 904
 846 277, doi:10.5194/cp-3-261-2007, 2007. 905
- 847 Braconnot, P., Marzin, C., Grnégoin, L., Mosquet, E., and Marti, 906
 848 O.: Monsoon response to changes in Earth’s orbital param- 907
 849 eters: comparisons between simulations of the Eemian and of the 908
 850 Holocene, *Clim. Past*, 4, 281–294, doi:10.5194/cp-4-281-2008, 909
 851 2008. 910
- 852 Chen, G.S., Kutzbach, J.E., Gallimore, R., Liu, Z.: Calen- 911
 853 dar effect on phase study in paleoclimate transient simula- 912
 854 tion with orbital forcing, *Climate Dyn.*, 37.9–10: 1949–1960, 913
 855 doi:10.1007/s00382-010-0944-6, 2011. 914
- 856 Collins, W. D., Bitz, C. M., Blackmon, M. L., Bonan, G. B., 915
 857 Bretherton, C. S., Carton, J. A., Chang, P., Doney, S. C., 916
 858 Hack, J. J., Henderson, T. B., Kiehl, J. T., Large, W. G., 917
 859 McKenna, D. S., Santer, B. D., and Smith, R. D.: The Com- 918
 860 munity Climate System Model version 3 (CCSM3), *J. Climate*, 919
 861 19, 2122–2143, doi: 110.1175/JCLI3761.1, 2006. 920
- 862 Crucifix, M., Loutre, F. M.: Transient simulations over the last inter- 921
 863 glacial period (126–115 kyr BP): feedback and forcing analysis, 922
 864 *Clim. Dyn.*, 19, 417–433, 2002 923
- 865 Dallmeyer, A., Claussen, M., Fischer, N., Haberkorn, K., Wagner, 924
 866 S., Pfeiffer, M., Jin, L., Khon, V., Wang, Y., and Herzsuh, 925
 867 U.: The evolution of sub-monsoon systems in the Afro-Asian 926
 868 monsoon region during the Holocene comparison of different 927
 869 transient climate model simulations, *Clim. Past*, 11, 305–326, 928
 870 doi:10.5194/cp-11-305-2015, 2015. 929
- 871 Davis, B. A. S. and Brewer, S.: astronomical forcing and role 930
 872 of the Latitudinal Insolation/Temperature Gradient, *Clim. Dyn.*, 931
 873 32, 143–165, doi: http://dx.doi.org/10.1007/s00382-008-0480- 932
 874 910.1007/s00382-008-0480-9, 2009. 933
- 875 deMenocal, P. B., Ruddiman, W. F., and Pokras, E. K.: In- 934
 876 fluences of high- and low-latitude processes on African cli- 935
 877 mate: Pleistocene eolian records from equatorial Atlantic Ocean 936
 878 Drilling Program Site 663, *Paleoceanography*, 8, 209–242, 937
 879 doi:10.1029/93PA02688, 1993. 938
- 880 deMenocal, P. B.: Plio-Pleistocene African climate, *Science*, 270, 939
 881 53–59, doi:10.1126/science.270.5233.53, 1995. 940
- de Noblet, N., Braconnot, P., Joussaume, S., and Masson, V.: Sensi-
 tivity of simulated Asian and African boreal summer monsoons
 to astronomically induced variations in insolation 126, 115 and
 6 kBP, *Clim. Dyn.*, 12, 589–603, 1996.
- Dutton, A. and Lambeck, K.: Ice Volume and Sea Level During the
 Last Interglacial, *Science*, 337, 216–219, 2012.
- Dutton, A., Carlson, A. E., Long, A. J., Milne, G. A., Clark, P.
 U., DeConto, R., Horton, B. P., Rahmstorf, S., Raymo, M. E.:
 Sea-level rise due to polar ice-sheet mass loss during past warm
 periods, *Science*, 349, doi: 10.1126/science.aaa4019, 2015.
- Erb, M. P., Broccoli, A. J., and Clement, A. C.: The contribution of
 radiative feedbacks to astronomically driven climate change, *J.*
Climate, 26, 5897–5914, 2013.
- Fischer, N. and Jungclauss, J. H.: Effects of astronomical forcing on
 atmosphere and ocean heat transports in Holocene and Eemian
 climate simulations with a comprehensive Earth system model,
Clim. Past, 6, 155–168, doi: 10.5194/cp-6-155-2010, 2010.
- Fleitmann, D., Burns, S. J., Mudelsee, M., Neff, U., Kramers, J.,
 Mangini, A., and Matter, A.: Holocene forcing of the Indian
 monsoon recorded in a stalagmite from Southern Oman, *Science*,
 300, 1737–1739, 2003.
- Gallimore, R. G. and Kutzbach, J. E.: Role of astronomically in-
 duced changes in tundra area in the onset of glaciation, *Nature*,
 381, 503–505, 1996.
- Govin, A., Varma, V., and Prange, M.: Astronomically forced vari-
 ations in western African rainfall (21° N–20° S) during the Last
 Interglacial period, *Geophys. Res. Lett.*, 41, 2117–2125, doi:
 10.1002/2013GL058999, 2014.
- Handiani, D., Paul, A., Prange, M., Merkel, U., Dupont, L., and
 Zhang, X.: Tropical vegetation response to Heinrich Event 1
 as simulated with the UVic ESCM and CCSM3, *Clim. Past*, 9,
 1683–1696, doi: 10.5194/cp-9-1683-2013, 2013.
- Hays, J. D., Imbrie, J., and Shackleton, N. J.: Variations in the
 Earth’s orbit: pacemaker of the Ice Ages, *Science*, 194, 1121–
 1132, 1976.
- Herold, N., Yin, Q. Z., Karami, M. P., and Berger, A.: Modelling
 the climatic diversity of the warm interglacials, *Quat. Sci. Rev.*,
 56, 126–141, doi: 10.1016/j.quascirev.2012.08.020, 2012.
- Hessler, I., Harrison, S. P., Kucera, M., Waelbroeck, C., Chen, M.-
 T., Anderson, C., de Vernal, A., Fréchet, B., Cloke-Hayes, A.,
 Leduc, G., and Londeix, L.: Implication of methodological un-
 certainties for mid-Holocene sea surface temperature reconstruc-
 tions, *Clim. Past*, 10, 2237–2252, doi: 10.5194/cp-10-2237-
 2014, 2014.
- Hoelzmann, P., Jolly, D., Harrison, S. P., Laarif, F., Bonnefille, R.,
 and Pachur, H. J.: Mid-Holocene land surface conditions in
 northern Africa and the Arabian Peninsula: a data set for the
 analysis of biogeochemical feedbacks in the climate system,
Global Biogeochem. Cy., 12, 35–52, 1998.
- IPCC: Climate Change 2001: The Scientific Basis. Contribution of
 Working Group I to the Third Assessment Report of the Inter-
 governmental Panel on Climate Change [Houghton, J.T., Ding,
 Y., Griggs, D. J., Noguer, M., van der Linden, P. J., Dai, X.,
 Maskell, K., and Johnson, C. A., (eds.)], Cambridge University
 Press, Cambridge, United Kingdom and New York, NY, USA,
 881pp, 2001.
- Jochum, M., Jahn, A., Peacock, S., Bailey, D. A., Fasullo, J. T.,
 Kay, J., Levis, S., and Otto-Bliesner, B.: True to Milankovitch:
 glacial inception in the new Community Climate System

- Model, *J. Climate*, 25, 2226–2239, doi: 10.1175/JCLI-D-11-1000-00044.1, 2012.
- Jouzel, J., Masson-Delmotte, V., Cattani, O., Dreyfus, G., Falourd, S., Hoffmann, G., Minster, B., Nouet, J., Barnola, J. M., Chappellaz, J., Fischer, H., Gallet, J. C., Johnsen, S., Leuenberger, M., Loulergue, L., Luethi, D., Oerter, H., Parrenin, F., Raisbeck, G., Raynaud, D., Schilt, A., Schwander, J., Selmo, E., Souchez, R., Spahni, R., Stauffer, B., Steffensen, J. P., Stenni, B., Stocker, T. F., Tison, J. L., Werner, M., and Wolff, E. W.: Climate variability over the past 800 000 years, *Science*, 317, 793–796, doi: 10.1126/science.1141038, Data archived at the World Data Center for Paleoclimatology, Boulder, Colorado, USA, 2007.
- Joussaume, S. and Braconnot, P.: Sensitivity of paleoclimate simulation results to season definitions, *J. Geophys. Res.*, 102, 1943–1956, 1997.
- Kaspar, F. and Cubasch, U.: Simulation of the Eemian interglacial and possible mechanisms for the glacial inception, *Geol. S. Am. S.*, 426, 29–41, 2007.
- Khodri, M., Cane, M. A., Kukla, G., Gavin, J., and Braconnot, P.: The impact of precession changes on the Arctic climate during the last interglacial-glacial transition, *Earth Planet. Sc. Lett.*, 236, 285–304, 2005.
- Kleinen, T., Hildebrandt, S., Prange, M., Rachmayani, R., Müller, S., Bezrukova, S., Brovkin, V., and Tarasov, P.: The climate and vegetation of Marine Isotope Stage 11 - model results and proxy-based reconstructions at global and regional scale, *Quatern. Int.*, 348, 247–265, doi: 10.1016/j.quaint.2013.12.028, 2014.
- Kopp, R. E., Simons, F. J., Mitrovica, J. X., Maloof, A. C., and Oppenheimer, M.: Probabilistic assessment of sea level during the last interglacial stage, *Nature*, 462(7275), 863–868, 2009.
- Kroon, D., Alexander, I., Little, M., Lourens, L. J., Matthewson, A., Robertson, A. H., and Sakamoto, T.: Oxygen isotope and sapropel stratigraphy in the eastern Mediterranean during the last 3.2 million years, *Proceedings of the Ocean Drilling Program, Scientific Results*, 160, 181–189, 1998.
- Kubatzki, C., Montoya, M., Rahmstorf, S., Ganopolski, A., Claussen, M.: Comparison of a coupled global model of intermediate complexity and an AOGCM for the last interglacial, *Clim. Dyn.*, 16, 799–814, 2000.
- Lang, N. and Wolff, E. W.: Interglacial and glacial variability from the last 800 kyr in marine, ice and terrestrial archives, *Clim. Past*, 7, 361–380, doi:10.5194/cp-7-361-2011, 2011.
- Levis, S., Bonan, G. B., Vertenstein, M., and Oleson, K. W.: The Community Land Models Dynamic Global Vegetation Model (CLM-DGVM): Technical Description and User's Guide, NCAR Technical Note NCAR/TN-459+IA, National Center for Atmospheric Research, Boulder, CO, 2004.
- Lisiecki, L. E. and Raymo, M. E.: A Pliocene-Pleistocene stack of 57 globally distributed benthic $\delta^{18}\text{O}$ records, *Paleoceanography*, 20, PA1003, doi: 10.1029/2004PA001071, 2005.
- Liu, Z., Zhu, J., Rosenthal, Y., Zhang, X., Otto-Bliesner, B. L., Timmermann, A., Smith, R. S., Lohmann, G., Zheng, W., and Timm, O. E.: The Holocene temperature conundrum, *P. Natl. Acad. Sci. USA*, 111, E3501–E3505, doi:10.1073/pnas.1407229111, 2014.
- Lohmann, G., Pfeiffer, M., Laepple, T., Leduc, G., and Kim, J.-H.: A model–data comparison of the Holocene global sea surface temperature evolution, *Clim. Past*, 9, 1807–1839, doi:10.5194/cp-9-1807-2013, 2013.
- Lorenz, S. J. and Lohmann, G.: Acceleration technique for Milankovitch type forcing in a coupled atmosphere–ocean circulation model: method and application for the Holocene, *Clim. Dyn.*, 23, 727–743, 2004.
- Loulergue, L., Schilt, A., Spahni, R., Masson-Delmotte, V., Blunier, T., Lemieux, B., Barnola, J.-M., Raynaud, D., Stocker, T. F., and Chappellaz, J.: Orbital and millennial-scale features of atmospheric CH_4 over the past 800,000 years, *Nature*, 453, 383–386, 2008.
- Loutre, M. F., and Berger, A.: Marine Isotope Stage 11 as an analogue for the present interglacial, *Global and Planetary Change*, 36(3), 209–217, 2003.
- Lunt, D. J., Abe-Ouchi, A., Bakker, P., Berger, A., Braconnot, P., Charbit, S., Fischer, N., Herold, N., Jungclauss, J. H., Khon, V. C., Krebs-Kanzow, U., Langebroek, P. M., Lohmann, G., Nisanicioglu, K. H., Otto-Bliesner, B. L., Park, W., Pfeiffer, M., Phipps, S. J., Prange, M., Rachmayani, R., Renssen, H., Rosenbloom, N., Schneider, B., Stone, E. J., Takahashi, K., Wei, W., Yin, Q., and Zhang, Z. S.: A multi-model assessment of last interglacial temperatures, *Clim. Past*, 9, 699–717, doi: 10.5194/cp-9-699-2013, 2013.
- Lüthi, D., Le Floch, M., Bereiter, B., Blunier, T., Barnola, J.-M., Siegenthaler, U., Raynaud, D., Jouzel, J., Fischer, H., Kawamura, K., and Stocker, T. F.: High-resolution carbon dioxide concentration record 650,000–800,000 years before present, *Nature*, 453, 379–382, 2008.
- Mantsis, D. F., Clement, A. C., Broccoli, A. J., and Erb, M. P.: Climate feedbacks in response to changes in obliquity, *J. Climate*, 24, 2830–2845, 2011.
- Mantsis, D. F., Lintner, B. R., Broccoli, A. J., Erb, M. P., Clement, A. C., and Park, H. S.: The response of large-scale circulation to obliquity-induced changes in meridional heating gradients, *J. Climate*, 27, 5504–5516, 2014.
- Marzin, C., Braconnot, P., and Kageyama, M.: Relative impacts of insolation changes, meltwater fluxes and ice sheets on African and Asian monsoons during the Holocene, *Clim. Dyn.*, 41, 2267–2286, 2013.
- McClure, H. A.: Radiocarbon chronology of late Quaternary lakes in the Arabian Desert, *Nature*, 263, 755–756, 1976.
- Meissner, K. J., Weaver, A. J., Matthews, H. D., and Cox, P. M.: The role of land-surface dynamics in glacial inception: a study with the UVic Earth System Climate Model, *Clim. Dyn.*, 21, 519–537, 2003.
- Milker, Y., Rachmayani, R., Weinkauff, M. F. G., Prange, M., Raitzsch, M., Schulz, M., and Kučera, M.: Global and regional sea surface temperature trends during Marine Isotope Stage 11, *Clim. Past*, 9, 2231–2252, doi: 10.5194/cp-9-2231-2013, 2013.
- Murray-Wallace, C., V.: Pleistocene coastal stratigraphy, sealevel highstands and neotectonism of the southern Australian passive continental margin a review, *Journal of Quaternary Science*, 17(5–6), 469–489., 2002.
- Muri, H., Berger, A., Yin, Q., Karami, M., and Barriat, P. V.: The climate of the MIS-13 Interglacial according to HadCM3, *J. Climate*, 26, 9696–9712, 2013.
- Nikolova, I., Yin, Q., Berger, A., Singh, U. K., and Karami, M. P.: The last interglacial (Eemian) climate simulated by LOVECLIM and CCSM3, *Clim. Past*, 9, 1789–1806, doi: 10.5194/cp-9-1789-2013, 2013.

- Oleson, K. W., Niu, G. Y., Yang, Z. L., Lawrence, D. M., Thornton, P. E., Lawrence, P. J., Stockli, R., Dickinson, R. E. G., Bonan, B., Levis, S., Dai, A., and Qian, T.: Improvements to the Community Land Model and their impact on the hydrological cycle, *J. Geophys. Res.*, 113, G01021, doi:10.1029/2007JG000563, 2008.
- Otto-Bliesner, B. L., Tomas, R., Brady, E. C., Ammann, C., Kothavala, Z., and Clauzet, G.: Climate sensitivity of moderate and low-resolution versions of CCSM3 to preindustrial forcings, *J. Climate*, 19, 2567–2583, 2006.
- Otto-Bliesner, B. L., Rosenbloom, N., Stone, E. J., McKay, N. P., Lunt, D. J., Brady, E. C., Overpeck, J. T.: How warm was the last interglacial? New model-data comparisons, *Philos. Trans. R. Soc. London Ser. A*, 371, 20130097, doi:10.1098/rsta.2013.0097; pmid: 24043870, 2013.
- Prell, W. L. and Kutzbach, J. E.: Monsoon variability over the past 150,000 years, *J. Geophys. Res.*, 92, 8411–8425, 1987.
- Rachmayani, R., Prange, M., and Schulz, M.: North African vegetation–precipitation feedback in early and mid-Holocene climate simulations with CCSM3-DGVM, *Clim. Past*, 11, 175–185, doi: 10.5194/cp-11-175-2015, 2015.
- Raymo, M. E., Nisancioglu, K. H.: The 41 kyr world: Mikovitch’s other unsolved mystery, *Paleoceanography*, 18 (1), 1011, doi: 10.1029/2002PA000791, 2003.
- Raymo, M. E., Mitrovica, J. X.: Collapse of polar ice sheets during the stage 11 interglacial, *Nature*, 2012/03/22/print, 483, 7390, 453–456, 2012.
- Renssen, H., Driesschaert, E., Loutre, M.F., Fichet, T.: On the importance of initial conditions for simulations of the Mid-Holocene climate, *Clim. Past*, 2, 91–97, 2006.
- Renssen, H., Seppä, H., Heiri, O., Roche, D. M., Goosse, H., and Fichet, T.: The spatial and temporal complexity of the Holocene thermal maximum, *Nat. Geosci.*, 2, 411–414, 2009.
- Schilt, A., Baumgartner, M., Blunier, T., Schwander, J., Spahni, R., Fischer, H., and Stocker, T. F.: Glacial–interglacial and millennial–scale variations in the atmospheric nitrous oxide concentration during the last 800,000 years, *Quat. Sci. Rev.*, 29, 182–192, 2010.
- Sitch, S., Smith, B., Prentice, I. C., Arneth, A., Bondeau, A., Cramer, W., Kaplan, J. O., Levis, S., Lucht, W., Sykes, M. T., Thonicke, K., and Venevsky, S.: Evaluation of ecosystem dynamics, plant geography and terrestrial carbon cycling in the LPJ dynamic vegetation model, *Glob. Change Biol.*, 9, 161–185, 2003.
- Tiedemann, R., Sarnthein, M., and Shackleton, N. J.: Astronomic timescale for the Pliocene Atlantic $\delta^{18}\text{O}$ and dust flux records of Ocean Drilling Program Site 659, *Paleoceanography*, 9, 619–638, 1994.
- Timm, O., Timmermann, A., Abe-Ouchi, A., Saito, F., and Segawa, T.: On the definition of seasons in paleoclimate simulations with orbital forcing, *Paleoceanography*, 23, PA2221, doi:10.1029/2007PA001461, 2008.
- Trenberth, K. E., Stepaniak, D. P., and Caron, J. M.: The global monsoon as seen through the divergent atmospheric circulation, *J. Climate*, 13, 3969–3993, 2000.
- Tuenter, E., Weber, S., Hilgen, F., and Lourens, L.: The response of the African boreal summer monsoon to remote and local forcing due to precession and obliquity, *Global Planet. Change*, 36, 219–235, 2003.
- Tzedakis, P. C., Hooghiemstra, H., and Palike, H.: The last 1.35 million years at Tenaghi Philippon: revised chronostratigraphy and long-term vegetation trends, *Quat. Sci. Rev.*, 25, 3416–3430, 2006.
- Tzedakis, P. C., Raynaud, D., McManus, J. F., Berger, A., Brovkin, V., and Kiefer, T.: Interglacial diversity, *Nat. Geosci.*, 2, 751–755, 2009.
- van Nes, E. H., Scheffer, M., Brovkin, V., Lenton, T. M., Ye, H., Deyle, E., and Sugihara, G.: Causal feedbacks in climate change, *Nature Climate Change*, 5, 445–448, doi: 10.1038/nclimate2568, 2015.
- Varma, V., Prange, M., Merkel, U., Kleinen, T., Lohmann, G., Pfeifer, M., Renssen, H., Wagner, A., Wagner, S., and Schulz, M.: Holocene evolution of the Southern Hemisphere westerly winds in transient simulations with global climate models, *Clim. Past*, 8, 391–402, doi: 10.5194/cp-8-391-2012, 2012.
- Wang, P. X., Wang, B., Cheng, H., Fasullo, J., Guo, Z. T., Kiefer, T., and Liu, Z. Y.: The global monsoon across timescales: coherent variability of regional monsoons, *Clim. Past*, 10, 2007–2052, doi: 10.5194/cp-10-2007-2014, 2014.
- Yeager, S. G., Shields, C. A., Large, W. G., and Hack, J. J.: The low-resolution CCSM3, *J. Climate*, 19, 2545–2566, 2006.
- Yin Q. Z., and Berger, A.: Interglacial analogues of the Holocene and its natural near future, *Quat. Sci. Rev.*, 20, 2015.
- Yin, Q. Z. and Berger, A.: Individual contribution of insolation and CO_2 to the interglacial climates of the past 800,000 years, *Clim. Dyn.*, 38, 709–724, 2012.
- Yin, Q., Berger, A., Driesschaert, E., Goosse, H., Loutre, M. F., and Crucifix, M.: The Eurasian ice sheet reinforces the East Asian summer monsoon during the interglacial 500 000 years ago, *Clim. Past*, 4, 79–90, doi: 10.5194/cp-4-79-2008, 2008.
- Yin, Q. Z., Berger, A., and Crucifix, M.: Individual and combined effects of ice sheets and precession on MIS-13 climate, *Clim. Past*, 5, 229–243, doi: 10.5194/cp-5-229-2009, 2009.
- Yin, Q. Z. and Berger, A.: Insolation and CO_2 contribution to the interglacial climate before and after the Mid-Brunhes Event, *Nat. Geosci.* 3, 243–246, doi: 10.1038/ngeo771, 2010.
- Zheng, W. and Braconnot, P.: Characterization of Model Spread in PMIP2 Mid-Holocene Simulations of the African Monsoon, *J. Climate*, 26, 1192–1210, 2013.

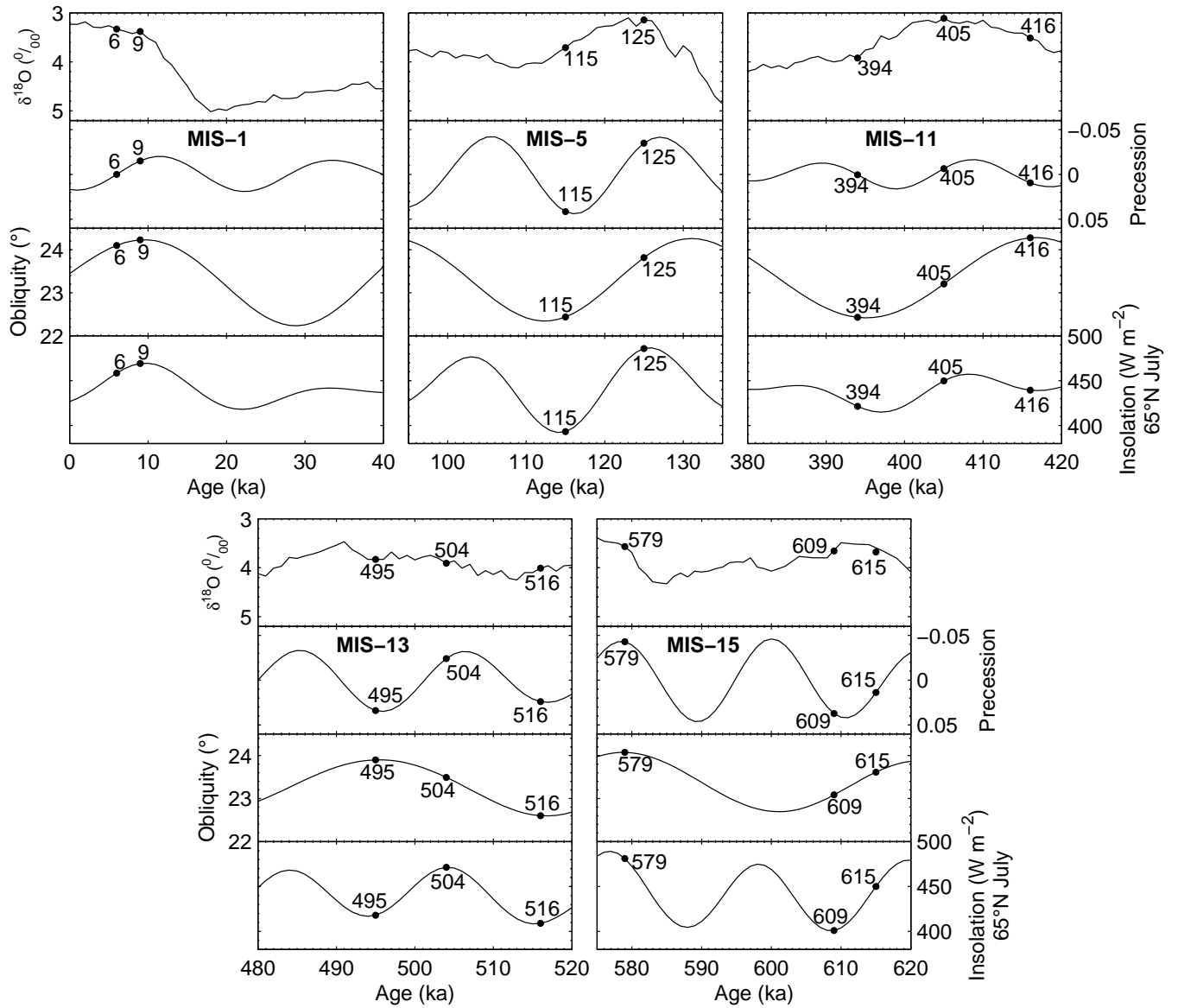


Figure 1. Benthic $\delta^{18}\text{O}$ stack (Lisiecki and Raymo, 2005), climatic precession, obliquity, and insolation at July, 65°N (Berger, 1978) for the different interglacials. The points mark the time slices simulated in this study.

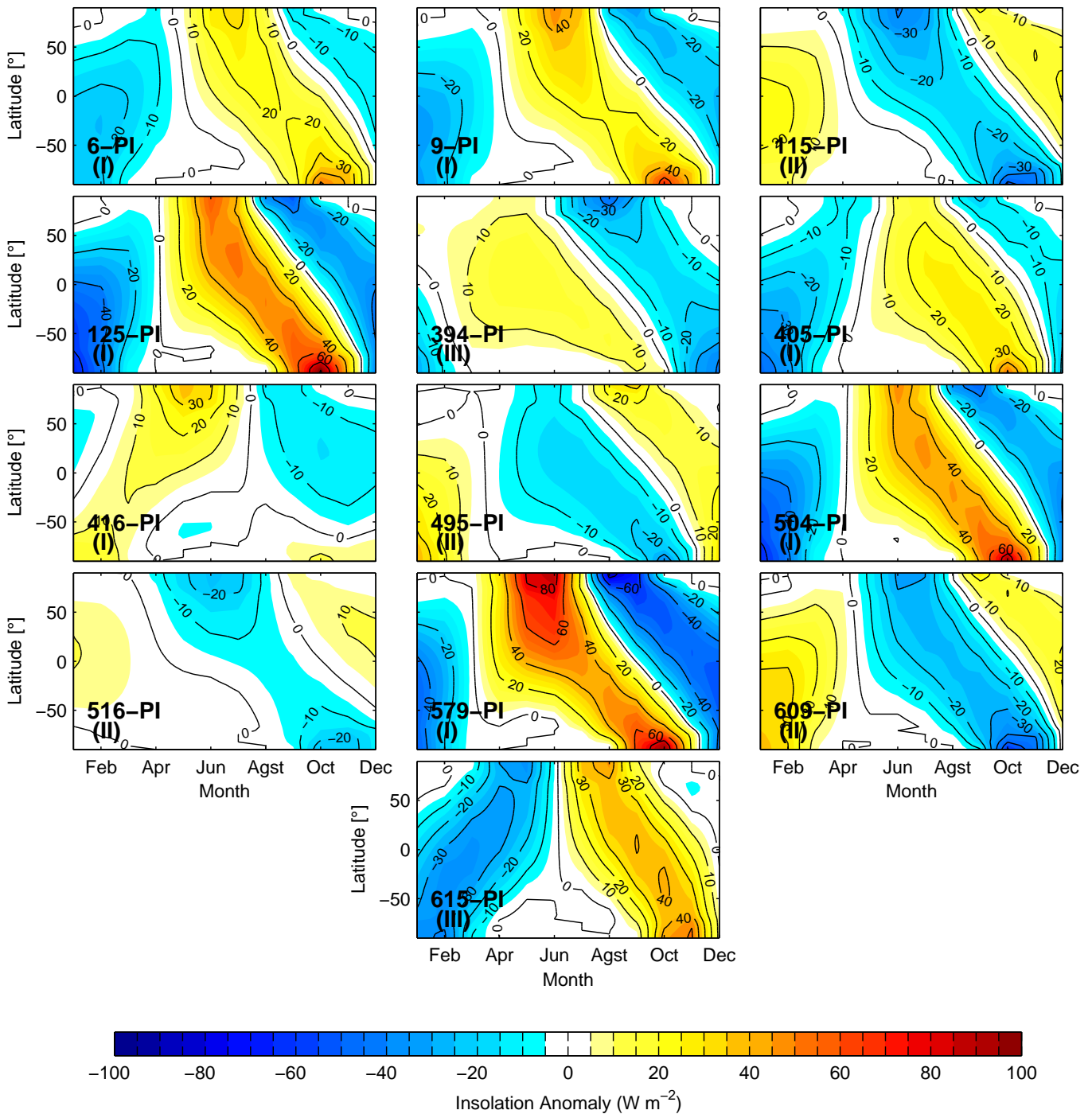


Figure 2. Insolation anomalies (relative to PI) for the time slices simulated in this study. Patterns of insolation anomaly are classified into Groups I, II, and III (see text). The calculation assumes a fixed present-day calendar with vernal equinox at 21 March.

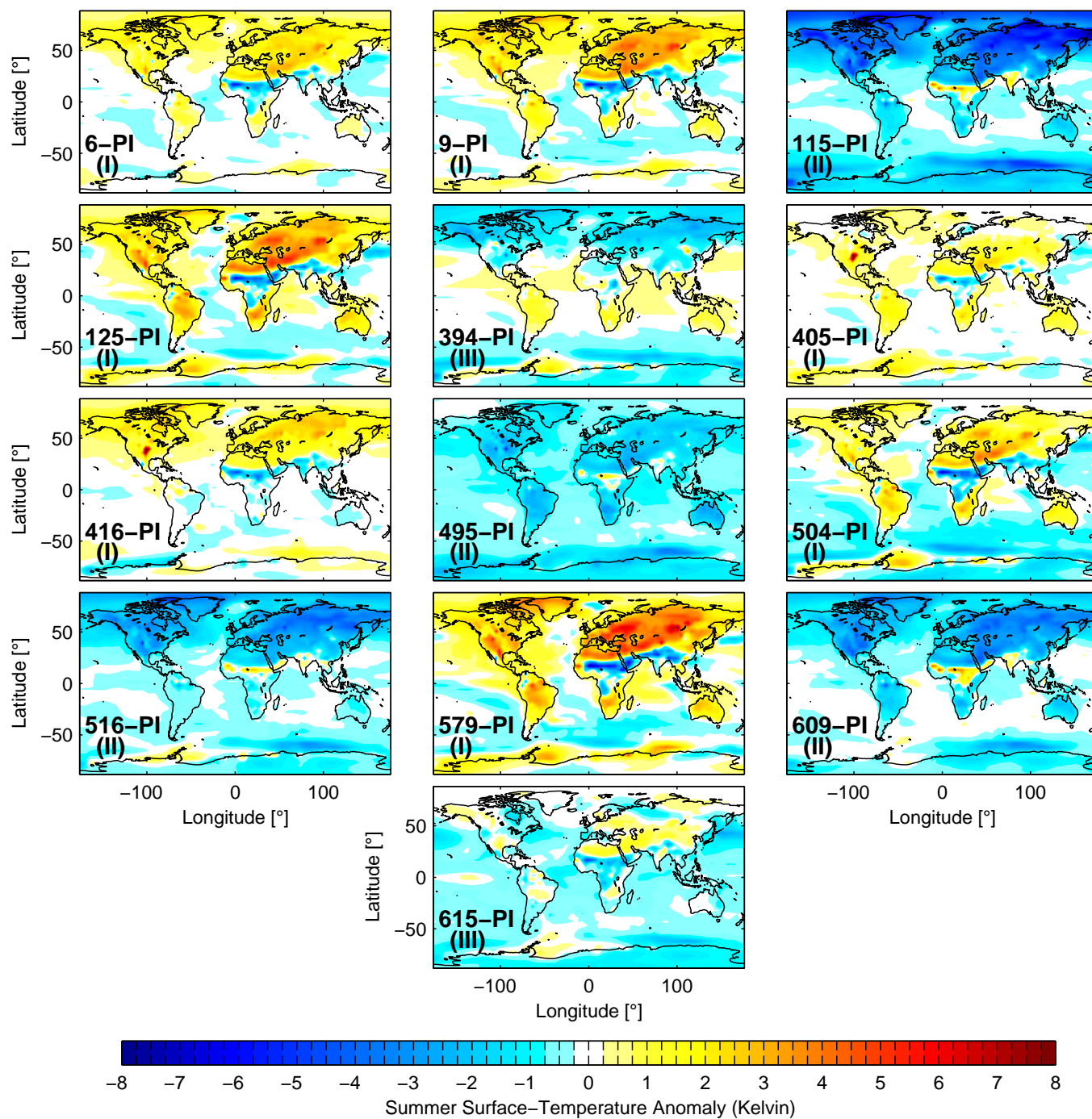


Figure 3. Boreal summer surface temperature anomalies (relative to PI) for the different interglacial time slices. Classification into Groups I, II, and III (see text) is indicated.

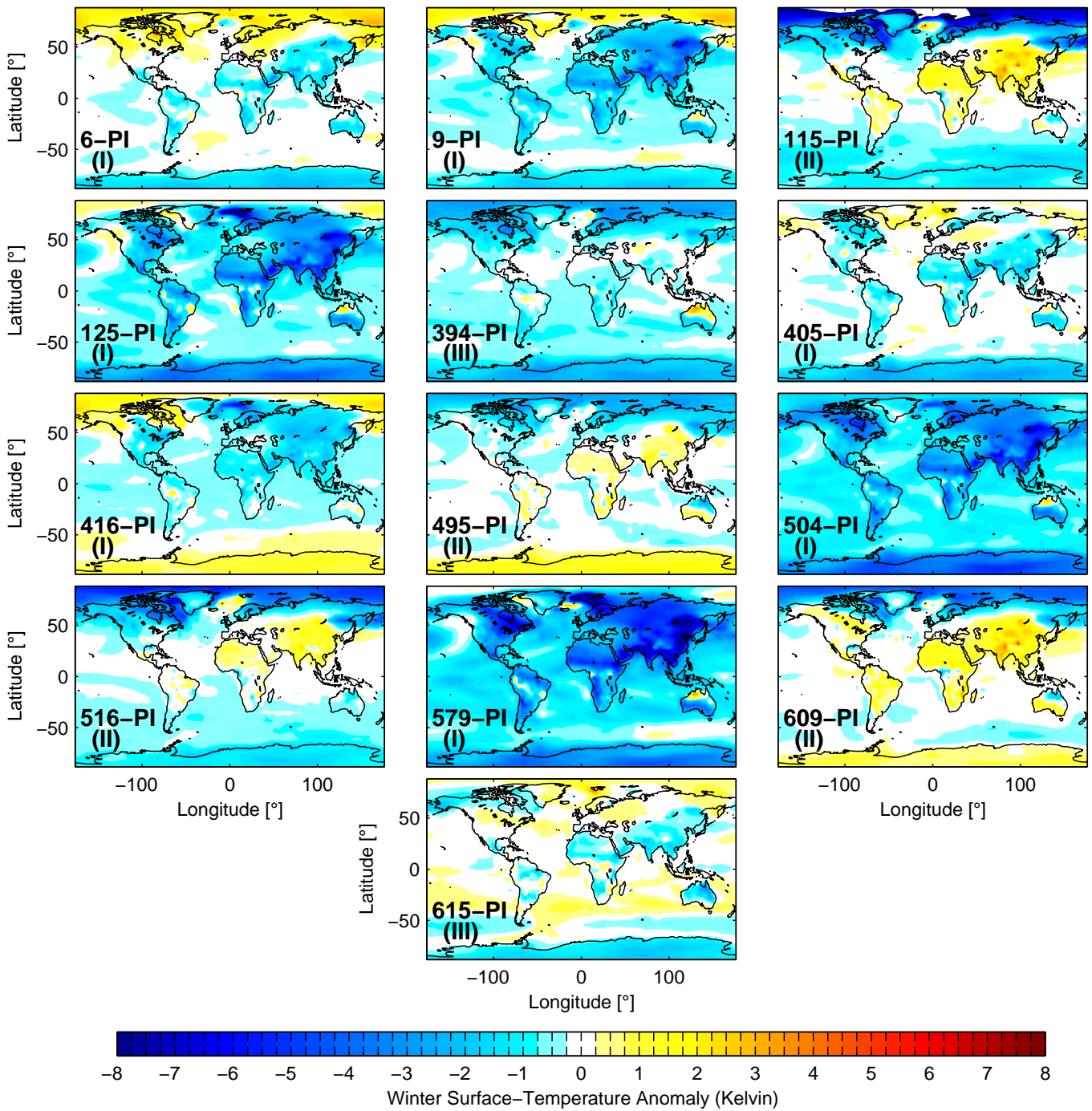


Figure 4. As in Fig. 3, but for boreal winter.

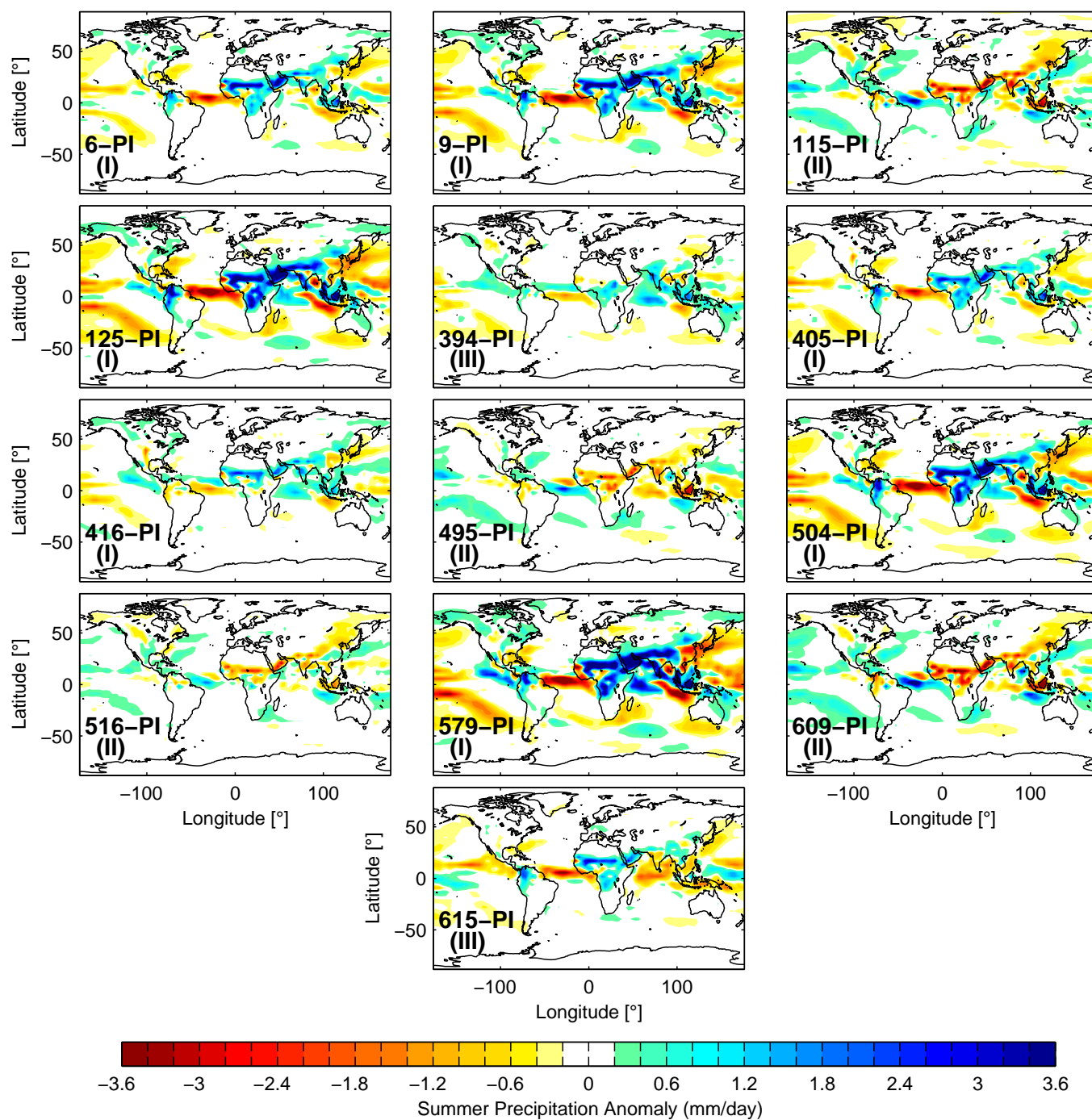


Figure 5. As in Fig. 3, but for boreal summer precipitation.

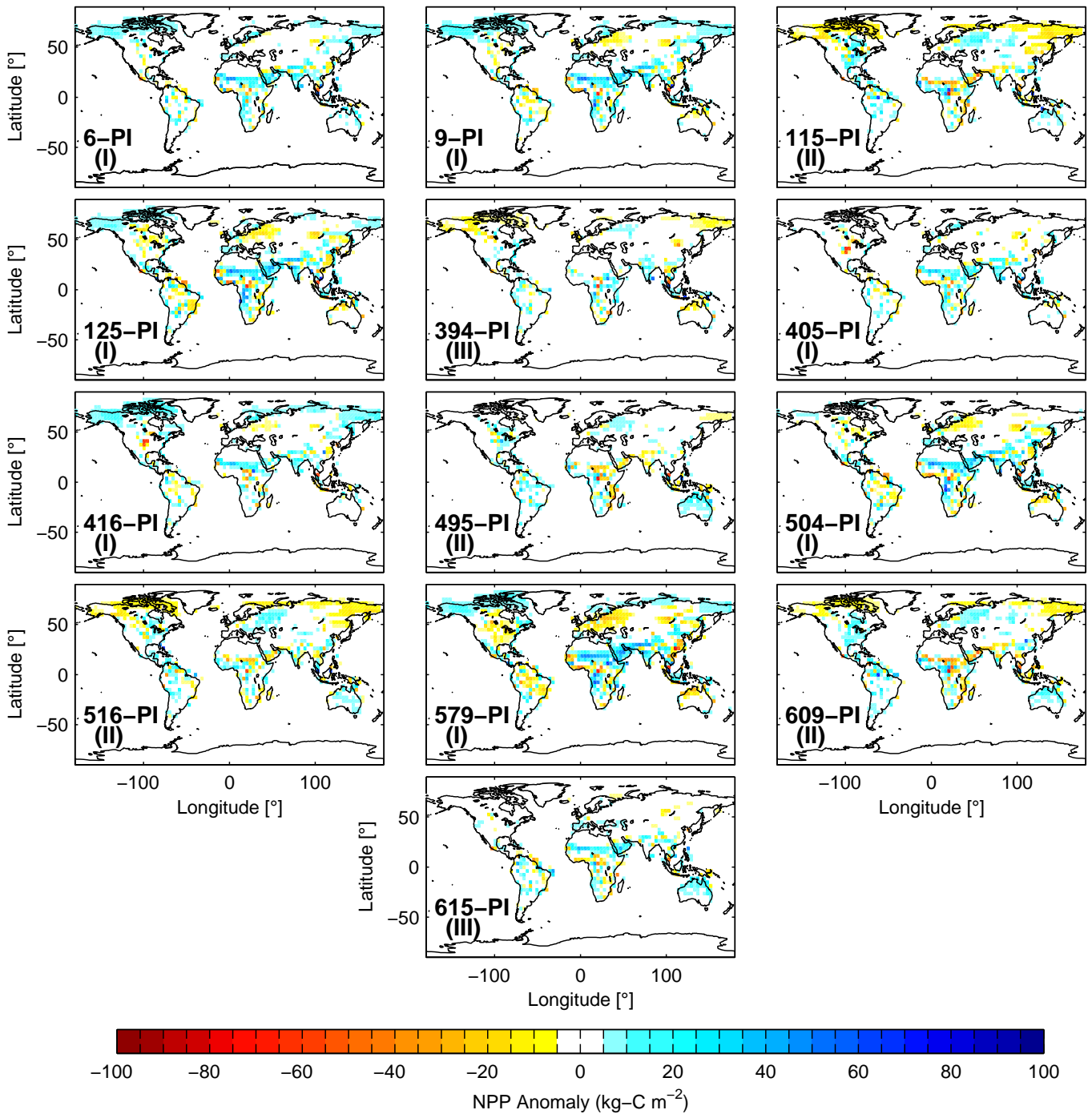


Figure 6. As in Fig. 3, but for annual net primary production.

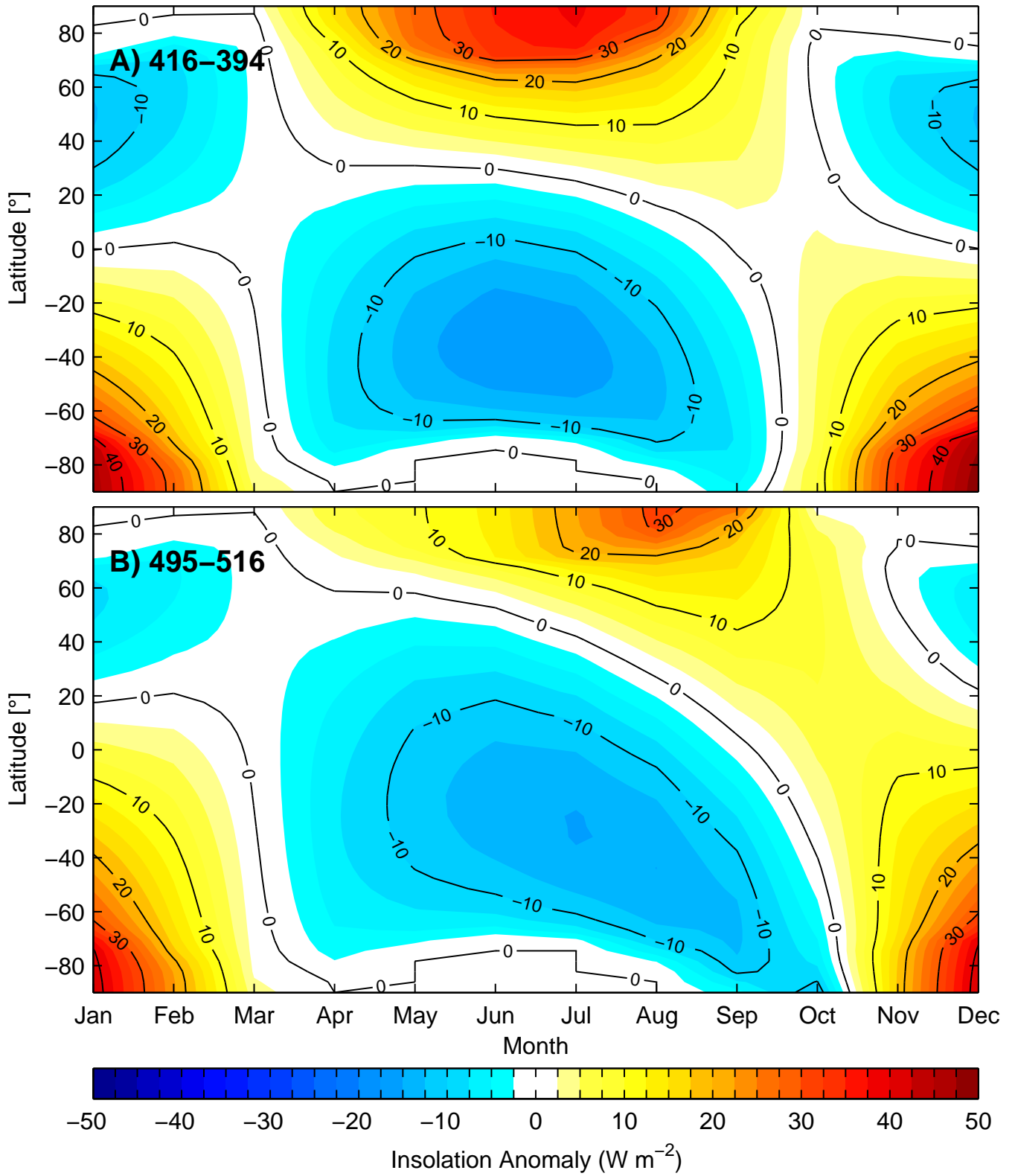


Figure 7. Differences in the seasonal and latitudinal distribution of insolation for (A) 416-394 ka BP, (B) 495-516 ka BP.

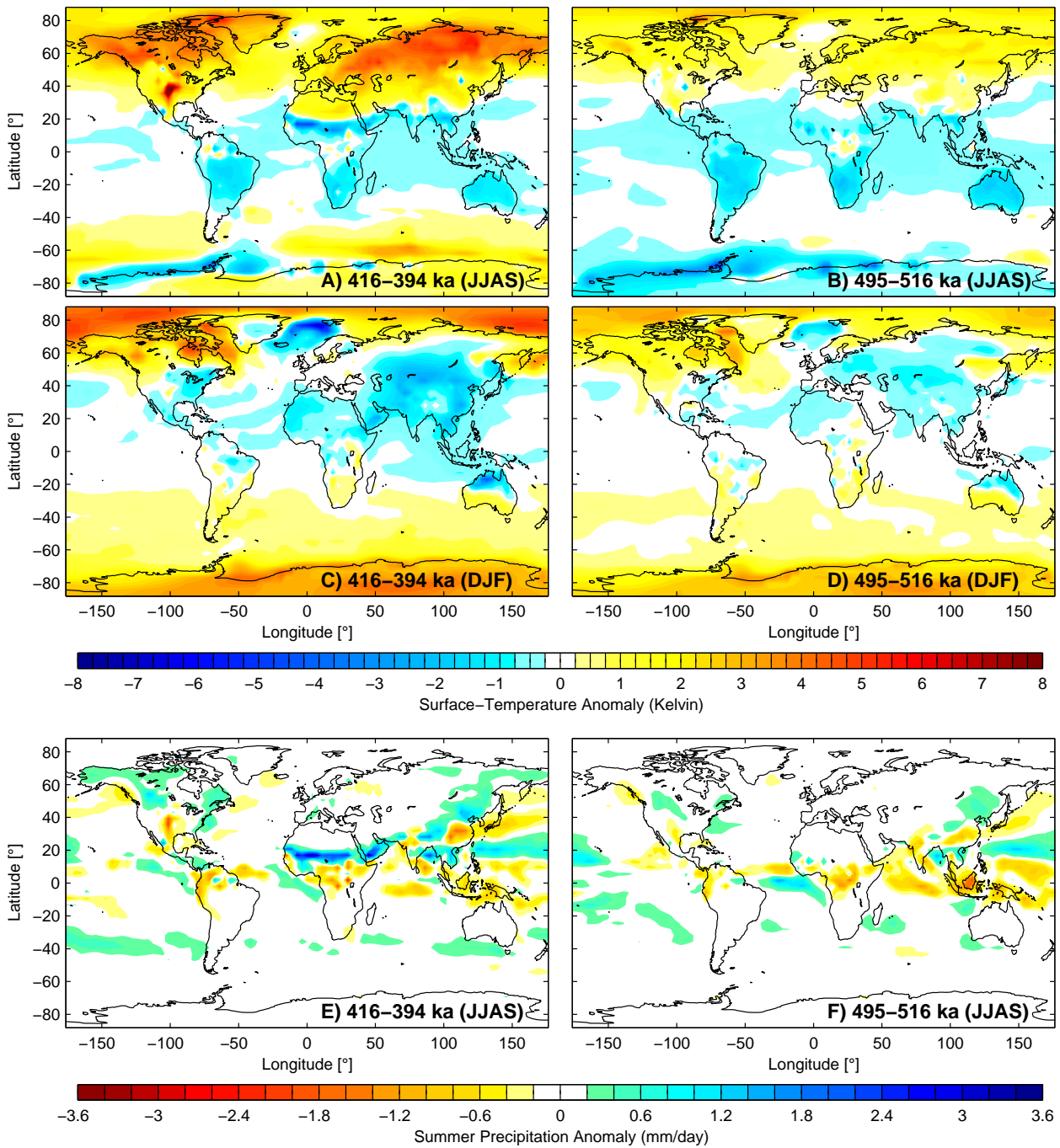


Figure 8. Differences in seasonal surface temperature (A)–(D) and boreal summer precipitation (E)–(F) for 416–394 ka BP (left) and 495–516 ka BP (right).

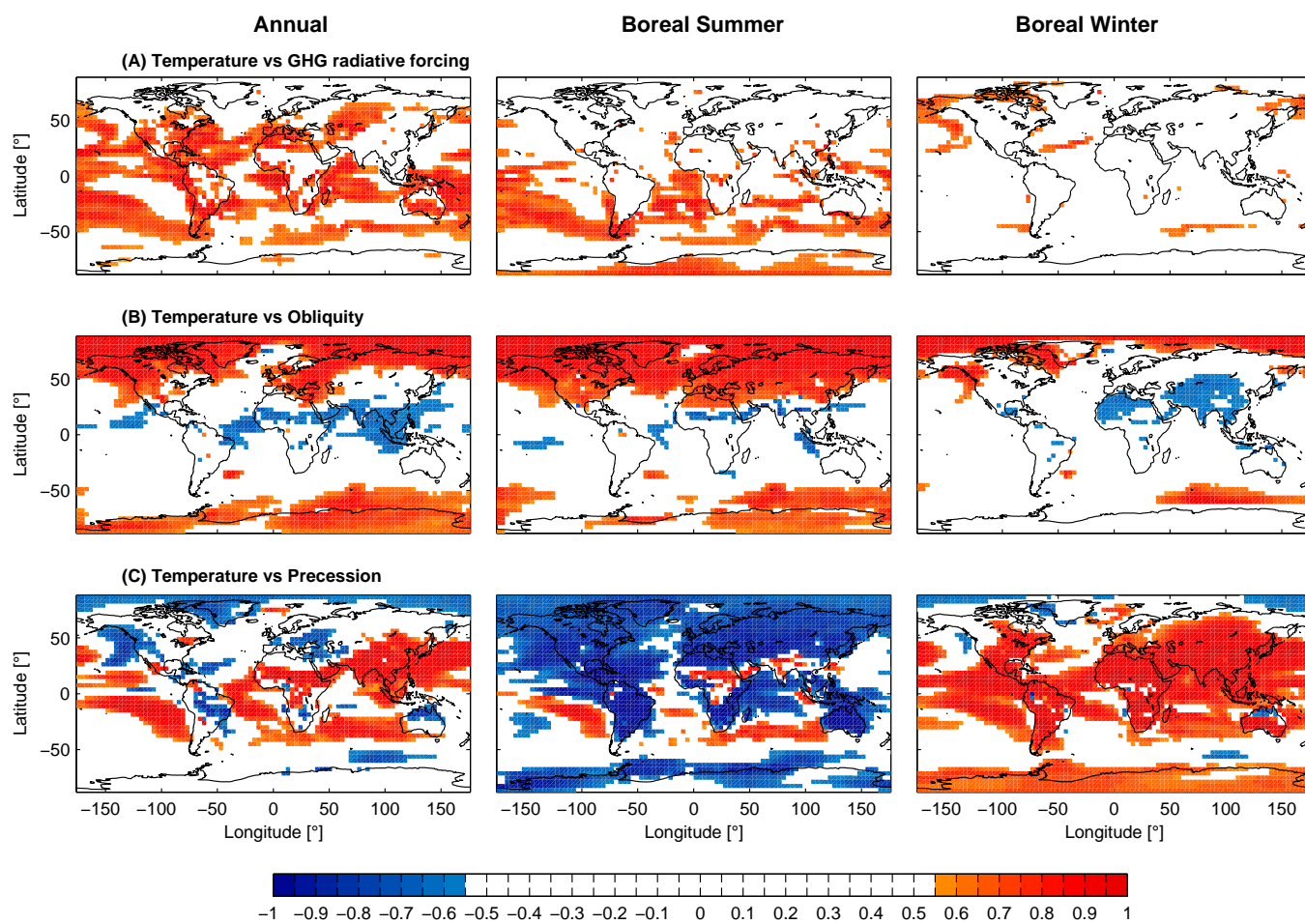


Figure 9. Linear correlation maps between surface temperature and GHG radiative forcing (A), obliquity (B), and climatic precession (C) as calculated from the entire set of experiments. Summer refers to JJAS, winter to DJF. Only significant values are shown according to a two-sided Student’s t-test at 95% confidence level.

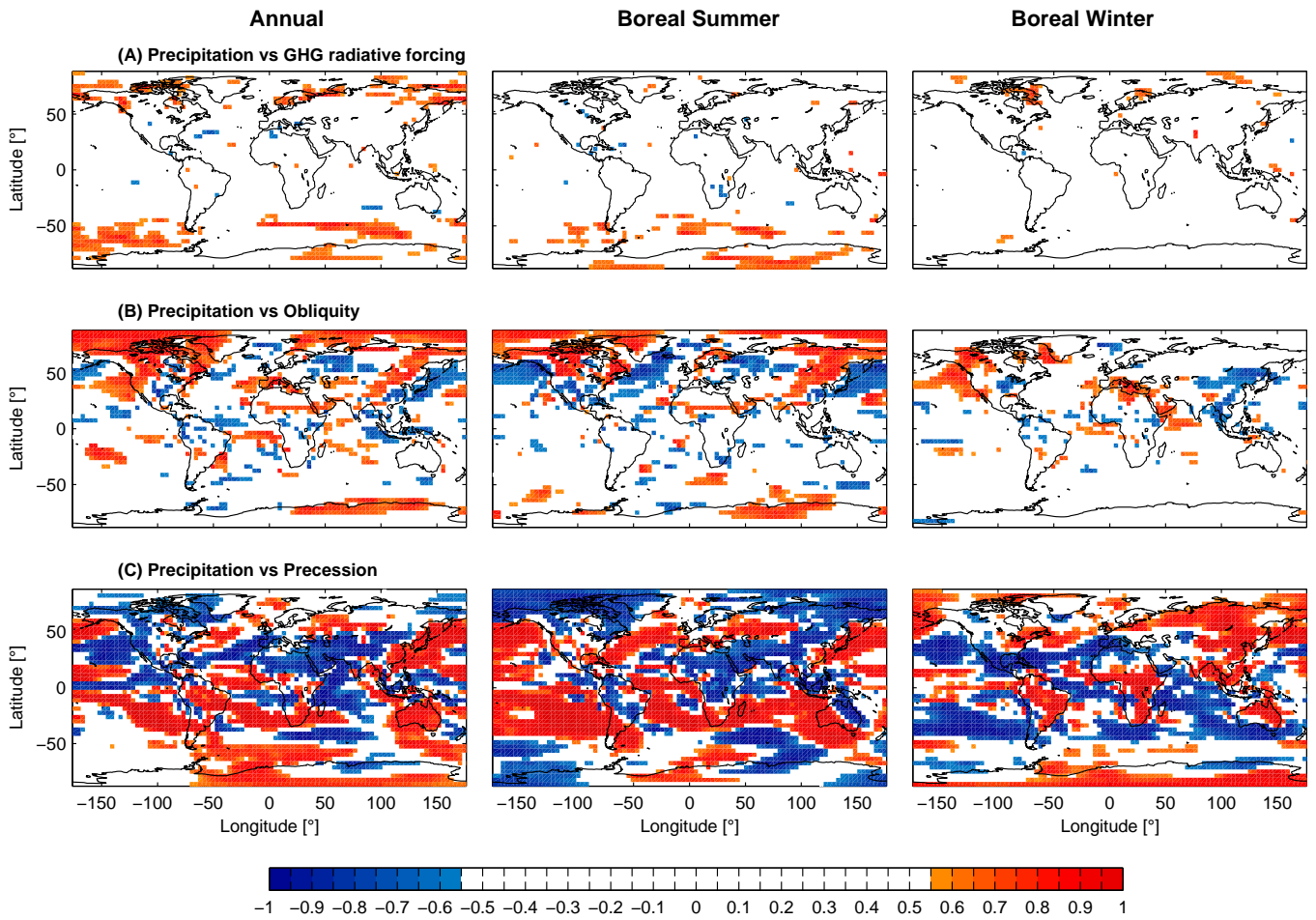


Figure 10. As in Fig. 9, but for precipitation.